MPA 1280e

Can three-flavour oscillations solve the solar neutrino problem?

H. Schlattl*
Max-Planck-Institut für Astrophysik, Karl-Schwarzschild-Str. 1, 85741 Garching, Germany
(May 5, 2000)

submitted to Physical Review D

The good agreement of standard solar models with helioseismology and the combined analysis of the solar neutrino experiments suggest that the solution to the solar neutrino problem is located in particle physics rather than in astrophysics. The most promising solution are neutrino oscillations with which the measured event rates in the detectors can be reproduced fairly well. However, in the scope of 2-flavour oscillations no parameter set can be found which reproduces the recent data of Super-Kamiokande about the electron-recoil energy spectrum, zenith-angle and seasonal variations and all the event rate data simultaneously. In this work a survey of the complete parameter space of three-flavour oscillations is performed, identifying basically six new additional solutions. The two best ones with $\Delta m^2_{12} = 3.3 \times 10^{-6}\,\mathrm{eV}^2$, $\Delta m^2_{13} = 1.1 \times 10^{-5}\,\mathrm{eV}^2$, $\Theta_{12} = 153°$ and $\Theta_{13} = 1.7°$ (denoted SHMA) and $\Delta m^2_{12} = 4.4 \times 10^{-10}\,\mathrm{eV}^2$, $\Delta m^2_{13} = 1.7 \times 10^{-5}\,\mathrm{eV}^2$, $\Theta_{12} = 32°$ and $\Theta_{13} = 1.1°$ (SVO) are slightly more probable than any 2-flavour solution. Including the constraints from the atmospheric neutrino problem ($\Delta m^2_{23} \approx 10^{-3}\,\mathrm{eV}^2$) excludes, however, all the three-flavour solutions, favoring the two-flavour LMA-solution. The relatively weak improvement of the fit using three-flavour instead of two-flavour oscillations, which appears to be due to an inconsistency of the different kind of data, indicates that there are probably systematic errors in at least one data set. In addition, the ability of SNO and Borexino to discriminate the various two- and three-flavour solutions is investigated. Only with very good statistics in these experiments the correct solution to the solar neutrino problem can be identified unambiguously.

*e-mail address: schlattl@mpa-garching.mpg.de

I. INTRODUCTION

From the beginning of the first measurements of the solar neutrino flux on Earth [1] until the present time, the origin of the solar neutrino problem could not yet be resolved totally. While previously inaccurate or unknown physics used in solar-model calculations could have been made responsible for the discrepancy between measured and predicted solar neutrino flux, this kind of solution can presently almost be ruled out, basically of two reasons:

Firstly, the high precision in the measurements of the solar p-mode frequencies and the development of helioseismological inversion techniques enable the determination of the solar sound-speed profile with high accuracy [2]. The comparison with standard solar models containing improved input physics like opacity, equation of state and microscopic diffusion shows an excellent agreement with the seismic models [3–5]. Predictions for the event rates in the solar neutrino detectors deduced from these standard solar models still are inconsistent with the measurements, confirming the solar neutrino problem (Table II).

Secondly, the three types of currently operating experiments, the chlorine detector [1], the gallium experiments GALLEX [6] and SAGE [7] and the Čerenkov counter Super-Kamiokande have different neutrino-energy thresholds. This allows to determine the contribution of different parts of the solar neutrino spectrum to the total flux without explicitly taking into account solar-model calculations. From this analysis it has been inferred that the experimental results can be explained only with huge changes in the nuclear fusion rates. The best fit with the data is obtained even with a *negative* flux of neutrinos created in the electron-capture process of ^{7}Be [8]. Nevertheless, strong modifications of the reaction cross sections would be difficult to explain experimentally and theoretically. Moreover, even if a presently unknown physical process can account for the demanded changes, the resulting solar models would hardly be consistent with helioseismology [9].

The most promising approach to the solution of the solar neutrino problem is an extension to the particle-physics standard model — neutrino mixing. Analogous to the CKM-mixing in the quark sector, weak and mass eigenstates of the neutrinos are supposed not to be identical but connected by a unitary transformation.

Under this assumption an initial solar electron-neutrino can be converted during its propagation to the Earth into another flavour, a μ- or τ-neutrino (*just-so* oscillations [10]). Furthermore, the neutrinos may coherently scatter forward in solar matter (*MSW-effect* [11]) altering the conversion probability for a certain set of mixing parameters.

The possible values for the mixing parameters, with which the measured event rates in all detectors can be reproduced simultaneously, have been derived by various authors [12,13]. But only the oscillations between two flavours usually is taken into account, as this case is already sufficient to explain the recorded rates.

However, recently Super-Kamiokande has published more detailed information about the energy distribution of the recoiled electrons and zenith-angle dependence of the neutrino-signal [14,15]. Follow-up investigations showed that it is not possible to explain satisfactorily these data *and* the event rates of all detectors by one set of mixing parameters (see [16] or section IV A): An excess of event rates in the high-energy bins seems to be inconsistent with the other data.

One possible explanation for the unexpected high number of events in the high-energy bins would be an enhanced flux of neutrinos produced in the proton-capture of ^{3}He. In this reaction the most energetic solar neutrinos are produced, but standard solar models predict that their flux is negligible small. To explain the Super-Kamiokande data the reaction rate for the ^{3}He+p-process must be about 20 times higher at least than theoretically evaluated [17], which is an order of magnitude bigger than the uncertainties in these calculations. Another explanation for this excess are systematic errors in the calibration of the electron energy as shown in [18].

In this work a different approach is followed. Since the usual fits of the neutrino-mixing parameters are performed within the framework of two neutrino flavours, the general case of three-flavour oscillations is investigated without making any assumptions about the mass scale as, for instance, inspired by the atmospheric neutrino problem. The latter is taken in various publications [19,20] as a constraint to investigate three-flavour oscillations. But here, the aim is to examine whether the expansion to three flavours in fact can lead to acceptable fits to all kind of data with one set of parameters. The implications for the atmospheric neutrino puzzle are discussed afterwards.

In section II the equations for three-flavour oscillations are derived from the solution to the Klein-Gordon equation and the size of the parameter space is deduced. After describing the underlying solar model and the neutrino analysis in section III, the results for two-flavour and three-flavour oscillations are shown (section IV). Finally the ability of forthcoming experiments like SNO and Borexino to discriminate the various solutions are discussed (section V).

II. THEORY OF NEUTRINO OSCILLATIONS

In the following an overview of the basic equations for neutrino oscillations are provided with particular emphasis to the three-flavour case. A more thorough description can be found e.g. in [21] or [9].

A. Vacuum oscillations

If neutrinos have mass, a mixing matrix similar to the Kobayashi-Maskawa matrix in the quark sector can be developed

$$|\nu_\alpha\rangle \;=\; \begin{pmatrix} \nu_e \\ \nu_\mu \\ \nu_\tau \end{pmatrix} \;=\; \mathcal{U} \begin{pmatrix} \nu_1 \\ \nu_2 \\ \nu_3 \end{pmatrix} \;=\; \mathcal{U}\,|\nu_i\rangle, \qquad (1)$$

where $|\nu_\alpha\rangle$ denotes the weak and $|\nu_i\rangle$ the mass eigenstates. The unitary matrix $\mathcal{U}$ can be parameterized by

$$\mathcal{U} = \begin{pmatrix} 1 & 0 & 0 \\ 0 & c_{23} & s_{23} \\ 0 & -s_{23} & c_{23} \end{pmatrix} \begin{pmatrix} c_{13} & 0 & s_{13}e^{-i\delta} \\ 0 & 1 & 0 \\ -s_{13}e^{i\delta} & 0 & c_{13} \end{pmatrix} \times \begin{pmatrix} c_{12} & s_{12} & 0 \\ -s_{12} & c_{12} & 0 \\ 0 & 0 & 1 \end{pmatrix} \qquad (2)$$

where s_{ij} and c_{ij} are abbreviations for $\sin\Theta_{ij}$ resp. $\cos\Theta_{ij}$ $(0 \le \Theta_{ij} < \pi/2)$ and δ is a CP-violating phase [22]. The equation of motion for a neutrino beam in vacuum obeys the Klein-Gordon equation for free particles ($\hbar = c = 1$)

$$(\partial_t^2 - \nabla^2 + M^2)\,|\nu_i(t,\vec{r})\rangle \;=\; 0, \qquad (3)$$

where the mass matrix M^2 is defined as

$$M^2 = \begin{pmatrix} m_1^2 & 0 & 0 \\ 0 & m_2^2 & 0 \\ 0 & 0 & m_3^2 \end{pmatrix}$$

with m_i being the mass of the neutrino mass eigenstate ν_i. Generally the solution is given by a superposition of plane waves $e^{i(\vec{k}\vec{r}-\omega t)}$ with the dispersion relation

$$\omega^2 = \vec{k}^2 + m^2.$$

In the case of the Sun with an almost stationary neutrino flux, $|\nu_i(t,\vec{r})\rangle$ can be expanded in components of fixed frequency $|\nu_i(\vec{r})\rangle_\omega\, e^{-i\omega t}$. For a spherically symmetric flux of relativistic neutrinos ($k \approx \omega$) one finally gets

$$-i\frac{\partial}{\partial r}|\nu_i(r)\rangle_\omega \;=\; \left(\omega - \frac{M^2}{2\omega}\right)|\nu_i(r)\rangle_\omega. \qquad (4)$$

The constant "potential" ω can be removed by shifting the energy scale, and by using $t = r$ Eq. (4) can be formally written as a more familiar Schrödinger-type equation

$$i\frac{\partial}{\partial t}|\nu_i(t)\rangle = \mathcal{H}|\nu_i(t)\rangle \qquad (5)$$

with $\mathcal{H} = E_{\rm kin} \approx \frac{M^2}{2\omega}$. The general solution to this equation is

$$|\nu_i(t)\rangle_\omega \;=\; e^{-it\frac{M^2}{2\omega}}\,|\nu_i(t_0)\rangle_\omega. \qquad (6)$$

The probability $P(r)_{\alpha\to\beta}$ to detect a neutrino ν_α with energy $E = \omega$ as a neutrino of type ν_β at distance $r = t$ from the source is therefore given by ($\mathcal{U}^{-1} = \mathcal{U}^\dagger$)

$$P(r)_{\alpha\to\beta} = \left|\,\langle\nu_\beta|\mathcal{U}e^{-ir\left(\frac{\Delta M^2}{2E}\right)}\mathcal{U}^\dagger|\nu_\alpha\rangle\,\right|^2. \qquad (7)$$

Using $\Delta m_{ij}^2 = m_j^2 - m_i^2$ the matrix ΔM^2 writes as

$$\Delta M^2 = M^2 - m_1^2\, Id_3 = \begin{pmatrix} 0 & 0 & 0 \\ 0 & \Delta m_{12}^2 & 0 \\ 0 & 0 & \Delta m_{13}^2 \end{pmatrix}.$$

With the mass eigenstate of an electron-neutrino being

$$\begin{pmatrix} \nu_1 \\ \nu_2 \\ \nu_3 \end{pmatrix}_{\rm e} \;=\; \mathcal{U}^\dagger \begin{pmatrix} 1 \\ 0 \\ 0 \end{pmatrix} \;=\; \begin{pmatrix} c_{12}c_{13} \\ s_{12}c_{13} \\ s_{13}e^{i\delta} \end{pmatrix}, \qquad (8)$$

Eq. (7) yields for the survival probability of ν_e's in vacuum

$$\begin{aligned} P(r)^{(3)}_{e\to e} = 1 &- \sin^2\left(\frac{\Delta m_{12}^2\, r}{4E}\right)\cos^4\Theta_{13}\,\sin^2 2\Theta_{12} \\ &- \left[\sin^2\left(\frac{\Delta m_{13}^2\, r}{4E}\right)\cos^2\Theta_{12} \right. \\ &\left. + \sin^2\left(\frac{\Delta m_{23}^2\, r}{4E}\right)\sin^2\Theta_{12}\right]\sin^2 2\Theta_{13}. \end{aligned} \qquad (9)$$

The superscript (3) denotes the case of three-flavour mixing. Since $P^{(3)}_{e\to e}$ does not depend on the CP-violating phase δ it is obvious that this quantity cannot be determined by considering neutrino oscillations. In the following, this term is thus omitted in the definition of U (Eq. 2). $P^{(3)}_{e\to e}$ depends on four quantities, two squared-mass differences, Δm_{12}^2 and Δm_{13}^2 ($\Delta m_{23}^2 = \Delta m_{13}^2 - \Delta m_{12}^2$), and two mixing angles Θ_{12} and Θ_{13}. The third mixing angle Θ_{23} does not appear in Eq. (8) and hence $P^{(3)}_{e\to e}$ is independent of this quantity. The survival probabilities for ν_μ and ν_τ depend on Θ_{23}, but its value cannot be determined by solar-neutrino experiments, as in the energy range of the solar neutrinos ν_μ and ν_τ interact equally with the detector material via NC-interactions. Thus, only the total number of μ- plus τ-neutrinos, given by $1-P^{(3)}_{e\to e}$, influences the event rate in detectors like Super-Kamiokande, SNO or Borexino.

For oscillations between two neutrino flavours where no mixing into the third flavour occurs (e.g. $\nu_e \leftrightarrow \nu_\mu$, $\Theta_{13} = 0$), Eq. (9) simplifies to the well known formula

$$P(r)^{(2)}_{e\to e} = 1 - \sin^2\left(\frac{\Delta m^2\, r}{4E}\right)\sin^2 2\Theta, \qquad (10)$$

where $\Delta m^2 = \Delta m_{12}^2$ or Δm_{13}^2 for ν_e-ν_μ– resp. ν_e-ν_τ–oscillations (Θ defined analogously).

B. Matter effect

During the propagation of the neutrinos through the Sun they coherently scatter forward on the particles of the solar plasma. Unlike μ- and τ-neutrinos, which only interact via NC-reactions, electron-neutrinos can in addition couple via $\mathcal{W}$-bosons to the electrons. Thus, the scattering cross section of a ν_e is altered as against the one of the other two neutrino-flavours. This can lead to a resonant flavour transition, which may create a pure ν_μ- or ν_τ-beam from the originally created electron-neutrinos, first theoretically postulated and described in [11] (*MSW-effect*).

This effect can be included in Eq. (5) by substituting $\mathcal{H}$ with $\tilde{\mathcal{H}} = \mathcal{H} + V_{\text{eff}}$, where

$$V_{\text{eff}} = \sqrt{2}\, G_F\, N_e\, \mathcal{U}^\dagger \begin{pmatrix} 1 & 0 & 0 \\ 0 & 0 & 0 \\ 0 & 0 & 0 \end{pmatrix} \mathcal{U}$$

influences solely the ν_e-contribution of the neutrino beam. G_F is the Fermi coupling-constant and N_e the electron number density. The new Hamiltonian $\tilde{\mathcal{H}}$ is no longer diagonal in the mass basis. To evaluate the survival probability and thus $\exp(-i\tilde{\mathcal{H}}t)$ it is therefore necessary to diagonalize $\tilde{\mathcal{H}}$ by a unitary transformation $\mathcal{V}$

$$\tilde{\mathcal{H}}_m = \begin{pmatrix} M_1 & 0 & 0 \\ 0 & M_2 & 0 \\ 0 & 0 & M_3 \end{pmatrix} = \mathcal{V}^\dagger \tilde{\mathcal{H}} \mathcal{V}.$$

Similar to the vacuum oscillations the constant phase $M_1\, Id_3$ can be removed from $\tilde{\mathcal{H}}$ as it does not change the survival probability. The complicated analytical expressions for ΔM_{ij} have been evaluated in [23]. Recently, $\exp(-i\tilde{\mathcal{H}}t)$ has been calculated in [24] by using Cayley-Hamilton's theorem without explicitly deriving $\mathcal{V}$. In the present work, however, $\mathcal{V}$ and M_i are computed with a fast numerical algorithm using none of the analytic expressions.

C. The parameter space

Recently various publications came up about the actual size of the necessary parameter space covering all possible solutions of the solar neutrino problem [25–27]. In this section the sometimes confusing statements about this topic are summarized and clarified.

The mixing angles can be defined to lie in the first quadrant by appropriately adjusting the neutrino field phases similar as in the quark sector [28]. This can also be verified from the final formulae, as, for instance, $P(r)^{(3)}_{e\to e}$ depends solely on the square of $\sin\Theta_{ij}$ resp. $\cos\Theta_{ij}$ ($ij = 12, 13$). Moreover, it has been shown in [25] that is is also sufficient to consider $0 \le \Theta_{23} < \pi/2$, if $P(r)^{(3)}_{e\to\mu}$ resp. $P(r)^{(3)}_{e\to\tau}$ are to be measured. In the case of the matter-enhanced oscillations the situation is not as trivial, but using an analytical formula for the evolution of a neutrino state in matter as derived in [24] (Eq. 44 therein), one can also show that the evolution of an initial electron-neutrino is determined only by the squares of $\sin\Theta_{ij}$ and $\cos\Theta_{ij}$.

1. Two flavours

First, the case of two-flavour oscillations is examined. Exchanging the first and second row in the definition of the mass eigenstates (Eq. 1) implies that $\Delta m^2 \to -\Delta m^2$ and $\sin\Theta \leftrightarrow \cos\Theta$ ($\Leftrightarrow \Theta \to (\pi/2-\Theta)$)†. Since the assignment of the masses m_i to the respective mass eigenstate ν_j must not change the results, e.g. the case $\Delta m^2 > 0$, $0 \le \Theta < \pi/4$ is equivalent to $\Delta m^2 < 0$, $\pi/4 \le \Theta < \pi/2$ for any possible form of the Hamiltonian. Thus, without loss of generality Θ can be chosen to be within $[0, \pi/4]$.

For pure vacuum oscillations Eq. (10) can be applied which yields that $P(r)^{(2)}_{e\to e}$ is independent of the sign of Δm^2 *and* under the transformation $\Theta \to (\pi/2 - \Theta)$. Hence, in this case it is even sufficient to consider $\Delta m^2 > 0$.

The situation is different for oscillations in matter, where the resonance condition for MSW-transition is given by

$$N_{\text{res}} = \frac{\Delta m^2/2E}{\sqrt{2}G_{\text{F}}} \cos 2\Theta. \tag{11}$$

A resonance may occur, if N_{res} is positive, thus $\Delta m^2 > 0$ ($\Theta \le \pi/4$). Although no resonance occurs for negative values of Δm^2, the matter still influences the evolution of the neutrino flavour composition in the solar interior (for a more detailed study see e.g. [23]).

In Fig. 1 the effect of solar matter on the energy dependence of $P^{(2)}_{e\to e}$ is demonstrated. For $E/|\Delta m^2| \lesssim 10^8\,\text{MeV/eV}^2$ vacuum oscillations would yield an energy-independent survival probability for electron-neutrinos, as the vacuum oscillation length is small and therefore only a mean value of (Eq. 10)

$$\langle P^{(2)}_{e\to e}\rangle_r = 1 - 0.5\sin^2 2\Theta \tag{12}$$

would be measurable on Earth. For $\sin^2 2\Theta = 0.7$ this leads to $\langle P^{(2)}_{e\to e}\rangle_r = 0.65$. In contrast to the case with $\Delta m^2 > 0$ (solid line), where the resonant flavour conversion diminishes the ν_e-contribution of the solar neutrino current, for $\Delta m^2 < 0$ (dashed line) the ν_e-portion is even enhanced compared to the pure vacuum-oscillation case. Thus, the minimum value of the ν_e-contribution for

†The indices 12 or 13 of the squared-mass difference resp. mixing angle are omitted in the two-flavour case.

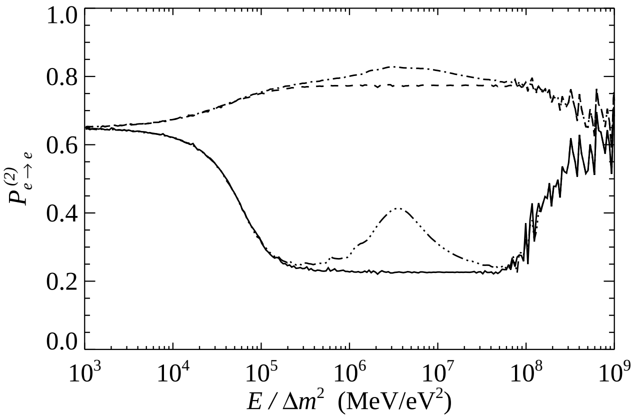

FIG. 1. Annually averaged probability of detecting a neutrino produced in the solar center as ν_e on Earth for $\sin^2 2\Theta = 0.7$ ($0 \le \Theta < \pi/4$) with $\Delta m^2 > 0$ (solid and dash-dot-dot-dotted) resp. $\Delta m^2 < 0$ (dashed and dash-dotted line). The two lines in each case show the probability neglecting (solid and dashed) resp. including (dash-dot-dot-dotted and dash-dotted) the Earth regeneration effect [30].

$\Delta m^2 < 0$ is obtained for pure vacuum oscillations. However, since vacuum oscillations in this mass range yield at most a suppression of the ν_e-flux of 50% (Eq. 12) and the solution to the solar neutrino problem demands, at least to explain the Homestake experiment, a stronger suppression of about 60%, for $\Delta m^2 < 0$ no reasonable solution can be obtained. Hence it is sufficient to consider in the two-flavour MSW case similar to the two-flavour vacuum oscillations solely $\Delta m^2 > 0$ ($\Theta \le \pi/4$).

Recently, it has been pointed out in [27,29] that the 3σ-ranges of the LMA- and LOW-solutions (see below) extend outside this region, but additional solutions for the solar neutrino problems cannot be found there. In their analysis, however, Δm^2 was fixed to be positive and thus $0 \le \Theta < \pi/2$ has been examined. The region $\pi/4 < \Theta < \pi/2$ of their parameter space (termed "the dark side") is equivalent to the region $\Delta m^2 < 0$ and $0 \le \Theta < \pi/4$ discussed above.

2. Three flavours

The considerations of the two-flavour case are now extended to three flavours. In Fig. 2 the flavour space for the electron-neutrino is illustrated, where ν_e is represented as a (yet unknown) point on the surface of an eight of an unit sphere. While in the two-flavour case the ordering of the masses enables two cases to be distinguished ($\Delta m^2 < 0$ resp. $\Delta m^2 > 0$), in the three-flavour scenario six cases can be identified. However, each of it can be obtained from the "canonical" hierarchy, i.e. $\Delta m_1^2 < \Delta m_2^2 < \Delta m_3^2$, by exchanging the respective assignment of m_i to ν_j in Eq. (1), which implies that also the respective axes in Fig. 2 have to be exchanged. Thus, all possible solutions are obtained by assuming a certain mass hierarchy and allowing Θ_{12} and Θ_{13} to vary within $[0, \pi/2]$ irrespectively of the exact form of the Hamiltonian.

Unlike the two-flavour case, where for pure vacuum oscillations the parameter space could be further decreased, it is not possible in the general three-flavour scenario, as e.g. $\Delta m_{23}^2 = \Delta m_{13}^2 - \Delta m_{12}^2$, is not invariant under the transformation $\Delta m_{12}^2 \to -\Delta m_{12}^2$.

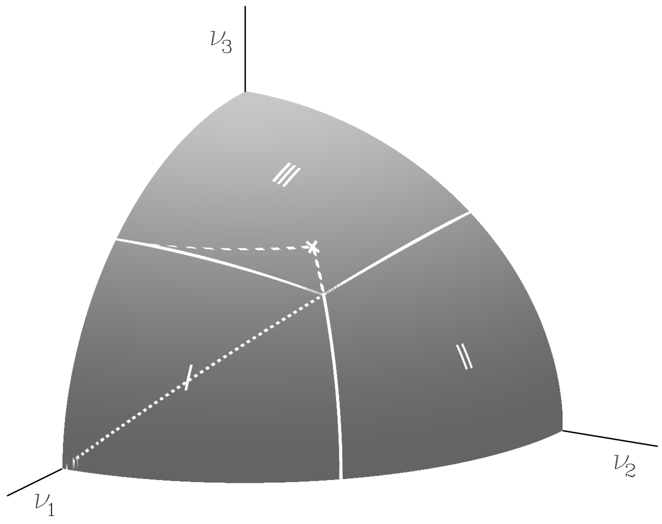

FIG. 2. Geometrical illustration of the flavour space available for a ν_e in the mass basis $(\nu_1, \nu_2, \nu_3)^{\mathrm{T}}$. The spherical segment is divided into three sectors of equal size and shape, where each can be obtained from another by mirroring at the respective diagonal. Maximal mixing is given at the intersection of all three sector borders, i.e. $\sin^2 2\Theta_{12} = 1$ and $\sin^2 2\Theta_{13} = \frac{8}{9}$. The cross in sector III indicates the case $\sin^2 2\Theta_{12} = \sin^2 2\Theta_{13} = 1$, the dashed border extends sector I to the area with $\Theta_{12}, \Theta_{13} \le \pi/4$. The dotted line splits sector I into two symmetric parts. (See text for more details.)

For three-flavour neutrino oscillations in matter an exact analytic resonance condition can hardly be obtained because of the complicated formula for the mass eigenvalues ΔM_{ij}. If the masses are well separated, the two-flavour resonance condition (Eq. 11) can be applied for both systems by substituting the quantities $(\Delta m^2, \cos 2\Theta)$ by $(\Delta m_{12}^2 \cos\Theta_{13}, \cos 2\Theta_{12})$ resp. $(\Delta m_{13}^2, \cos 2\Theta_{13})$ [31]. Hence, in this case considering $\Theta_{12}, \Theta_{13} \le \pi/4$ (sector I extended to the dashed borders in sector III of Fig. 2) with $\Delta m_{12}^2, \Delta m_{13}^2 \ge 0$ is sufficient to obtain all possible solutions where two resonances may occur. However, the solution to the solar neutrino problem may also be a combination of a non-resonant and a resonant oscillation and the masses can be in principle very similar, too. Thus, the whole parameter space must be taken into account.

In [19], for instance, three-flavour oscillations were investigated assuming canonical mass hierarchy

$(m_1^2 < m_2^2 < m_3^2)$ and using a fixed value for $\Delta m_{13}^2 = 10^{-3}$ eV^2 in agreement with the atmospheric-neutrino results. They examined the remaining parameter space applying an analytical formula for the ν_e survival probability, which approximates the solar electron-density profile by an exponential function and is valid for $\Delta m_{13}^2 \approx 10^{-3}$ eV^2 and Δm_{12}^2 significantly smaller than Δm_{13}^2. Under these conditions the parameter space could be reduced considerably.

In the present work, the most general case of three-flavour oscillations of solar neutrinos is investigated, and thus these restrictions are not applicable here. Instead of making a survey over the whole flavour space ($0 \leq \Theta_{12}, \Theta_{13} < \pi/2$) with canonical mass hierarchy, I prefer to consider the case $\Delta m_{12}^2, \Delta m_{13}^2 > 0$ which covers two possible mass hierarchies. Thus, in this case only half of the total flavour space must be overviewed. In the illustration provided in Fig. 2 this reduced area is given by sector II and the lower half of sector I defined by the dotted line.

To simplify the numerical survey and the analysis a variable transformation to the mixing angles is applied in each sector: Obviously $P_{e\to e}^{(3)}$ as defined in Eq. (9) is not symmetric under the exchange of the indices $2 \leftrightarrow 3$. However, sector I is symmetric under $\nu_2 \leftrightarrow \nu_3$, and it would be useful to have two quantities $\tilde{\Theta}_{12}(\Theta_{12}, \Theta_{13})$ and $\tilde{\Theta}_{13}(\Theta_{12}, \Theta_{13})$ which fulfill

$$P_{e\to e}^{(3)}(\Delta m_{12}^2, \tilde{\Theta}_{12}, \Delta m_{13}^2, \tilde{\Theta}_{13}) = P_{e\to e}^{(3)}(\Delta m_{13}^2, \tilde{\Theta}_{13}, \Delta m_{12}, \tilde{\Theta}_{12}).$$

Defining in sector I ($0 \leq \Theta_{12} < \pi/4$, $\tan\Theta_{13} \leq \cos\Theta_{12}$) the quantities $\tilde{s}_{12} (= \sin\tilde{\Theta}_{12})$ and $\tilde{s}_{13}$ by

$$\begin{aligned} \tilde{s}_{12} &= s_{12} \\ \tilde{s}_{13} &= \frac{s_{13}}{\sqrt{1 - s_{12}^2 c_{13}^2}}, \end{aligned} \tag{13}$$

yields such a pair. With these quantities Eq. (9) writes as ($\tilde{c}_{ij}^2 = 1 - \tilde{s}_{ij}^2$)

$$P(r)_{e\to e}^{(3)} = 1 - \left(\frac{2\tilde{c}_{12}\tilde{c}_{13}}{1 - \tilde{s}_{12}^2\tilde{s}_{13}^2}\right)^2 \left[\tilde{s}_{12}^2\tilde{c}_{13}^2 \sin^2\left(\frac{\Delta m_{12}^2 r}{4E}\right) + \tilde{c}_{12}^2\tilde{s}_{13}^2 \sin^2\left(\frac{\Delta m_{13}^2 r}{4E}\right) + \tilde{s}_{12}^2\tilde{s}_{13}^2 \sin^2\left(\frac{\Delta m_{23}^2 r}{4E}\right)\right],$$

which is unaltered under the exchange of the indices $2 \leftrightarrow 3$.

Moreover, it can be proven that the evolution matrix of neutrinos in matter is not changed when exchanging the indices $2 \leftrightarrow 3$ [9]. Hence, using $\tilde{s}_{12}$ and $\tilde{s}_{13}$ in sector I yields a ν_e survival probability, which is constant under this transformation in vacuum as well as in matter.

Similar to sector I also sector II ($\pi/4 \leq \Theta_{12} < \pi/2$, $\tan\Theta_{13} \leq \sin\Theta_{12}$) can be brought in a quadratic shape by using the transformation

$$\tilde{s}_{13} = \frac{s_{13}}{\sqrt{1 - c_{12}^2 c_{13}^2}}. \tag{14}$$

But this does not yield a survival probability invariant under the exchange of the indices $2 \leftrightarrow 3$, as under this operation sector II would be mapped on sector III.

III. CALCULATIONS

A. Standard solar model

For the following calculations my standard solar model ("GARSOM4") as described in [32] is used. It has been calculated using the latest input physics, equation of state and opacity from the OPAL-group [33,34] and nuclear reaction rates as proposed by [35]. In addition, microscopic diffusion of H, ^{3}He, ^{4}He, the CNO-isotopes and 4 heavier elements (among them Fe) is included using the diffusion constants of [36]. By treating convection as a fast diffusive process the chemical changes due to nuclear burning and diffusion (mixing) are evaluated in a common scheme.

A peculiarity of GARSOM4 is the inclusion of realistic 2d-hydrodynamical model atmospheres [37] until an optical depth of 1000. The improvement of the high-degree p-mode frequencies due to a better reproduction of the superadiabatic layers just below the photosphere is similar to the one obtained by using 1d-model atmospheres like in [3]. The advantage of using the 2d- instead of the 1d-model atmospheres is the extension of the former to greater optical depths, where the stratification is already adiabatic and thus the solar model gets nearly independent of the applied convection theory.

In Table I typical quantities of GARSOM4 using the convection theory developed in [38] are summarized. The predicted event rates of GARSOM4 for the three presently operating types of neutrino experiments GALLEX/SAGE, Homestake and Super-Kamiokande are summarized in Table II together with the values obtained by [4]. Since the input physics is very similar in both models, the predicted rates agree very well within the errors as quoted by [4].

Figure 3 shows the sound-speed profile of GARSOM4 compared to the seismic model inferred by [42]. The

TABLE I. Typical quantities of GARSOM4. $\alpha_{\rm CM}$ is the mixing-length parameter of the convection theory developed in [38]. Y and Z are helium and metal mass fractions, T and ρ temperature and mass density, respectively. The depth of the convective envelope in units of the solar radius is abbreviated by $R_{\rm bce}$. The indices i, s and c denote initial, surface (photospheric) and central values.

$\alpha_{\rm CM}$	Y_i	Z_i	Y_s	Z_s	T_c (10^7 K)	ρ_c (g/cm^3)	$R_{\rm bce}$	$\rho_{\rm bce}$ (g/cm^3)
0.975	0.275	0.020	0.245	0.018	1.57	152	0.713	0.188

TABLE II. Expected event rates resp. neutrino flux in the three types of experiments GALLEX/SAGE (Ga), Homestake (Cl) and Super-Kamiokande as predicted by the two solar models GARSOM4 and BP98 [4]. In the last row the measured values with their respective errors are provided.

	Ga [SNU]	Cl [SNU]	Super-K [$10^6\mathrm{cm}^{-2}\mathrm{s}^{-1}$]
GARSOM4	128.4	7.58	5.06
BP98	129^{+8}_{-6}	$7.7^{+1.2}_{-1.0}$	$5.15^{+1.00}_{-0.72}$
Experiment	72.5 ± 5.6[a]	2.56 ± 0.23[b]	2.42 ± 0.08[c]

[a]Reference [39]
[b]Reference [40]
[c]Reference [41]

deviations of GARSOM4 from the latter are of the same size as standard solar models from other groups [4,43].

B. Neutrino-oscillation analysis

Using the neutrino flux as provided by GARSOM4 the evolution of the initial electron neutrinos through Sun, space and Earth is computed taking into account oscillations between the flavours (see Appendix). The electron-density profile and the radial distribution of the neutrinos is taken from the solar model, too. For the electron-density profile of the Earth the spherically symmetric PREM-model [45] is applied. For each set of mixing parameters the neutrino energy spectrum observed on Earth is evaluated and folded with the detector response functions. The combination of mixing parameters which reproduce the measured data are found by applying a χ^2-analysis.

There are four contributions to the total value of χ^2 originating from the four different available data sets, the event rates, the recoil-electron energy spectrum, the zenith-angle distribution and the annual variation. The latter three are available only from the Super-Kamiokande detector, while to the first one all three types of neutrino experiments contribute.

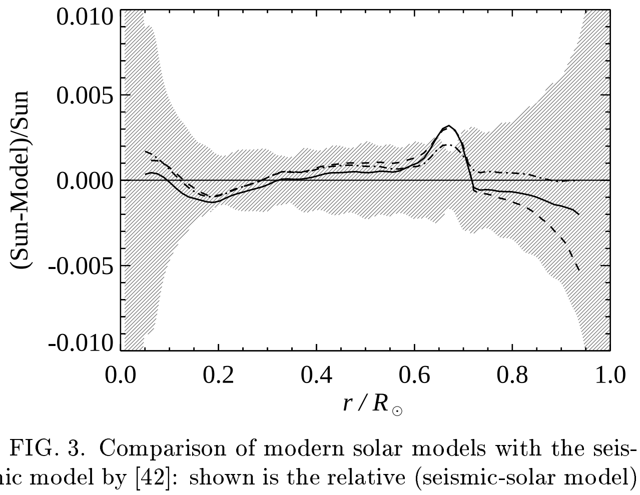

FIG. 3. Comparison of modern solar models with the seismic model by [42]: shown is the relative (seismic-solar model) difference of sound speed for the model of reference [4] (dashed line), reference [43] (dash-dotted) and GARSOM4 (solid). The grey-shaded area indicates a conservative error range of seismic models according to [44].

For the event-rate portion the commonly used formula holds

$$\chi^2_R = \sum_{i=1}^{3} \frac{\left(N_i^{\mathrm{exp}} - N_i^{\mathrm{th}}\right)^2}{\sigma^2_{i,\mathrm{exp}} + \sigma^2_{i,\mathrm{th}}}, \tag{15}$$

where i denotes GALLEX/SAGE, Homestake or Super-Kamiokande. σ^2_{exp} and σ^2_{th} are the experimental resp. theoretical 1σ-errors (Table II). Since the input physics in GARSOM4 is similar to the one used in [4], the theoretical errors derived therein are taken for σ^2_{th}. N_i^{exp} are the measured event rates, which are quoted together with the uncertainties in Table II. Note, that the Super-Kamiokande data are usually reported as ^{8}B-neutrino flux relatively to a standard solar-model prediction. Actually this number has to be understood as an event-rate ratio. The total number of measured events are divided by the theoretically expected value (e.g. from GARSOM4). This ratio is then often falsely taken to be the suppression rate of the *total* ^{8}B-neutrino flux. However, with the energy window of the recoiled electrons presently being between 5.5 and 20 MeV no statement about the total number of ^{8}B-neutrinos below this window is possible. Moreover, neutrino oscillations may alter the energy spectrum of the ^{8}B electron-neutrino flux and as the scattering cross section of the neutrinos in Super-Kamiokande is energy-dependent, the same number of event rates can be obtained with different ^{8}B-neutrino fluxes. In the present analysis therefore the event rate in Super-Kamiokande following Eq. (A5) are used and not the total ^{8}B-neutrino flux.

The recoil-electron spectrum is examined following [14] by

$$\chi^2_e = \sum_{i=1}^{18} \left[\frac{N_{i,e}^{\mathrm{exp}} - N_{i,e}^{\mathrm{th}} \frac{\alpha_e}{(1+\delta_{i,\mathrm{exp}}\beta)(1+\delta_{i,\mathrm{cal}}\gamma)}}{\sigma_{i,e}} \right]^2 + \beta^2 + \gamma^2, \tag{16}$$

where the sum extends over all 18 energy bins (Fig. 5(a)) and $\delta_{i,\mathrm{exp}}$ and $\delta_{i,\mathrm{cal}}$ are the 1σ-ranges of the correlated experimental errors resp. of the uncertainties in the calculation of the expected spectrum provided by the Super-Kamiokande collaboration [41]. $\sigma^2_{i,e}$ is obtained by quadratically adding the uncorrelated and statistical error in each energy bin. Since the absolute value of the event rate in Super-Kamiokande has already been used in χ^2_R the parameter α_e is introduced, by which the spectrum can be normalized adequately, independent of the total rates. Due to the very poor knowledge of correlations in the systematic errors between the bins, the additional parameters β and γ are included [14]. The actual χ^2_e-value for a certain set of theoretical determined binned event rates $N^{\rm th}_{i,e}$ is the minimum value obtained by numerically varying the parameters α_e, β and γ. By this method the influence of unknown systematic errors on the agreement of a predicted recoil-electron spectrum with the data should be diminished.

For the zenith-angle dependence (6 bins, Fig. 5(b)) the χ^2-term is defined as

$$\chi^2_Z = \sum_{i=1}^{6} \left(\frac{N^{\rm exp}_{i,Z} - \alpha_Z N^{\rm th}_{i,Z}}{\sigma_{i,Z}} \right)^2 , \qquad (17)$$

where σ^2_Z is the quadratic sum of statistical and systematic errors and α_Z is, similar to α_e, a normalization parameters chosen to minimize χ^2_Z. The contribution of the seasonal-variation data (4 bins, Fig. 5(c)) is defined analogously (denoted in the following χ^2_A)

IV. RESULTS

A. Two flavours

In a first step the solar neutrino problem is analyzed taking into account oscillations only between two flavours. Figure 4 shows the allowed oscillation parameters, if solely the event rates of the three experiments are fitted. Clearly the four commonly known solution-islands (see e.g. in [12,13]) can be identified, the small-mixing (SMA) and large-mixing angle (LMA), the low squared-mass difference (LOW) and the vacuum-oscillation (VO) solutions. The χ^2-values for the best-fit parameters in these solutions are quoted in Table III. Apart from LOW all solutions have a ratio of χ^2 to the number of degrees-of-freedom (d.o.f.) which is less than one and therefore these solutions are acceptable candidates as correct solution for the solar neutrino puzzle.

If, however, the recoil-electron energy spectrum, the zenith-angle and annual variations recorded by Super-Kamiokande are tried to be fitted simultaneously with the event rates, the situation is different. As also found e.g. in [18] no solution has a χ^2/d.o.f.-ratio less than one and hence, usually all are rejected as explanation to the solar neutrino problem.

In particular, only the VO-solution reproduces the measured recoil-electron spectrum reasonably well — $\chi^2_{\rm e}$/d.o.f. ≈ 1 (cf. Fig 5(a) and Table III). However, with $\chi^2_{\rm R} = 6.38$ this solution fails to predict the event rates.

By assuming that the Chlorine rate is due to unknown systematic errors 30% higher than quoted and by reducing the reaction rate for the ^{7}Be-proton capture by about 15–20%, a VO-solution could be obtained which would be able to reproduce the event rates *and* the recoil-electron spectrum of Super-Kamiokande fairly well [46]. However, presently there is no evidence for any hidden systematic uncertainties in Homestake, which would increase the event rate to the 3.5σ-level.

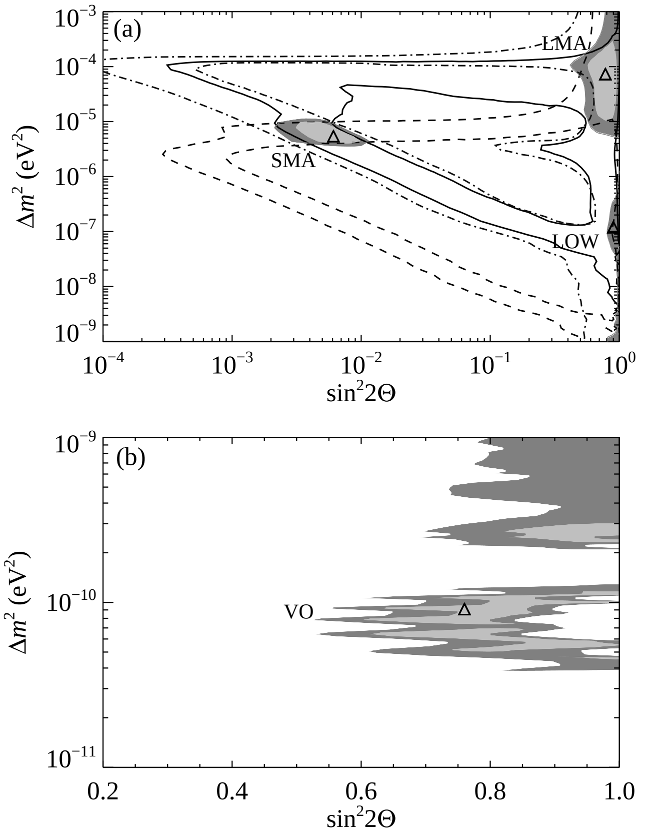

FIG. 4. Confidence regions in the Δm^2-$\sin^2 2\Theta$–plane for 2-flavour neutrino oscillations using only the event rates. Due to the different mass ranges and dependences on the mixing angle, the MSW-solutions are shown in (a), the pure vacuum-oscillation solutions in (b). The light shaded areas reflect the 95.4% C.L., while the dark shaded regions show the 99.7% C.L. Also drawn in (a) are the constraints from Homestake (solid), GALLEX/SAGE (dashed) and Super-Kamiokande (dash-dotted line). The best-fit value of each solution is indicated by $\triangle$ (Table III).

The parameters of the best-fit LMA-, SMA- and LOW-solutions are only weakly modified when including all the data in the analysis (Table III). Basically, because of the zenith-angle data a slight shift of the best-fit values of the LMA- and SMA-solution has occurred. Because the recoil-electron spectrum can hardly be reproduced by any mixing parameter in the mass range of the MSW-solutions, all these solutions have a very high $\chi^2_{\rm e}$-value and only small constraints are obtained from these data.

Since for $\Delta m^2 = 10^{-6} - 10^{-3}\,{\rm eV}^2$ only very small deviations from a constant neutrino flux are expected and this is consistent with the season data recorded by Super-Kamiokande ($\chi^2_{\rm A}/d.o.f. \approx 0.5$), the parameter spaces of the LMA- and SMA-solutions are only weakly restricted by this kind of data. For smaller Δm^2 a detectable annual variation may occur, and therefore this data set provides important limits on the parameter space of the LOW- and VO-solutions. Accidentally, the best-fit

TABLE III. Best fit values for neutrino oscillations between two neutrinos and the respective χ^2-values. In the first four rows, only the event rates are taken into account, while in the latter rows also the zenith-angle dependence, annual variation and recoil-electron spectrum data of Super-Kamiokande are included. χ^2_R, χ^2_e, χ^2_Z and χ^2_A are the individual contributions to $\chi^2_{\rm tot}$ as defined by Eqs. (15)–(17). The last row specifies the contribution of each χ^2-portion to the total number of d.o.f, the last column the available number of d.o.f of each fit.

	Δm^2 [eV^2]	$\sin^2 2\Theta$	χ^2_R	χ^2_e	χ^2_Z	χ^2_A	$\chi^2_{\rm tot}$	d.o.f.
SMA	5.4×10^{-6}	6.1×10^{-3}	0.18	—	—	—	0.18	1
LMA	7.3×10^{-5}	0.78	0.83	—	—	—	0.83	1
LOW	1.2×10^{-7}	0.90	3.82	—	—	—	3.82	1
VO	9.1×10^{-11}	0.76	0.49	—	—	—	0.49	1
SMA	7.8×10^{-6}	4.7×10^{-3}	0.98	25.6	8.0	1.7	36.3	24
LMA	3.5×10^{-5}	0.78	1.17	24.6	4.3	1.6	31.6	24
LOW	1.2×10^{-7}	0.90	3.82	24.3	6.2	0.6	35.0	24
VO	6.3×10^{-10}	1.00	6.38	18.3	8.6	1.4	34.6	24
d.o.f.			3	15	5	3		

LOW-solution of the pure-rate analysis already reproduces the recorded seasonal variation best and actually is also the best-fit LOW-solution in the full analysis.

In any case, the recoil-electron spectrum presently seems to be incompatible with the other kind of data sets, if neutrino oscillations are assumed. Thus, improved statistics in the recoil-electron spectrum data of Super-Kamiokande is required to identify more reliably neutrino oscillations as solution to the neutrino problem.

Nevertheless, by the LMA-solution currently the best fit to all measurements is obtained; the reason being, that the zenith-angle variation is reproduced much better as by the other solutions (Table III and Fig. 5(b)) confirming the results found in [18].

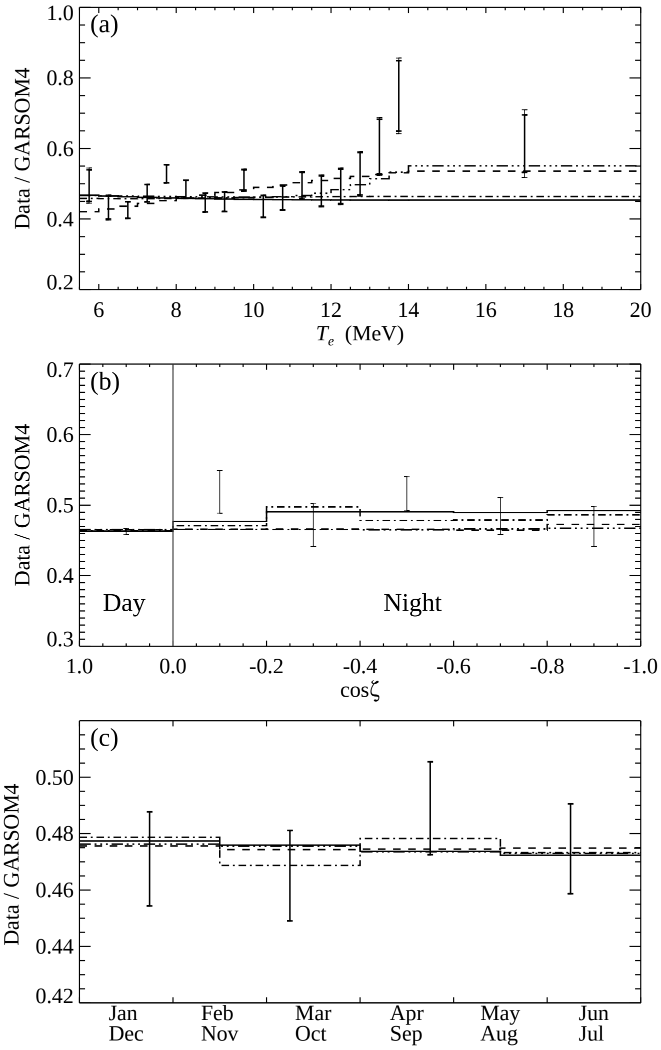

FIG. 5. Recoil-electron spectrum (a), zenith-angle (ζ) variation (b) and seasonal dependence of the best-fit LMA- (solid line), SMA- (dashed), LOW- (dash-dotted) and VO- (dash-dot-dot-dotted) solutions in the two-flavour oscillation case including all available solar neutrino data (Table III, lower part) compared with the measurements of Super-Kamiokande (708-days data [41]). All bins are equally spaced in the respective data area apart from the last bin in the energy spectrum, the range of which extends from 14 to 20 MeV. The flux variation due to the eccentric orbit of the Earth has been subtracted in (c).

B. Three flavours

Since the recoil-electron energy spectrum, the zenith-angle and seasonal variations and the event rates can be fitted only very poorly simultaneously in the two-flavour oscillation-scenario, in the following all three families are included into the analysis.

The electron-neutrino survival probability for three-flavour neutrino oscillations is determined by four quantities Δm^2_{12}, $\sin^2 2\Theta_{12}$, Δm^2_{13} and $\sin^2 2\Theta_{13}$, where the appropriate pairs describe each the mixing of two flavours. Hence a 4-dimensional parameter space has to be examined to deduce those sets of parameters, with which the experimental results can be reproduced. In the Appendix the numerical realization is described with which the 4-dimensional parameter survey can be performed efficiently. As worked out in section II C, all possible solutions for MSW-solutions are obtained by considering sector I and II (Fig. 2) with Δm^2_{12}, $\Delta m^2_{13} > 0$. In sector I, using $\sin^2 2\tilde{\Theta}_{13}$ as defined in Eq. (13) instead of $\sin^2 2\Theta_{13}$, allows to describe the pure two-neutrino ν_1-ν_3–oscillations equivalently to the ν_1-ν_2–case, which has been investigated thorougly in various publications [12,13]. In addition, with the survival probabilities $P(r)^{(3)}_{\rm e\to e}(\Delta m^2_{12}, \sin^2 2\Theta_{12}, \Delta m^2_{13}, \sin^2 2\tilde{\Theta}_{13})$ being symmetric in the exchange of the indices 2 and 3 unnecessary computations can be avoided. Nevertheless, the computations are very extensive due to the 4-dimensional parameter space. Therefore, the grid in the three-flavour oscillation-survey has to be chosen less dense than in the two-flavour case, where only a 2-dimensional grid had to be overviewed. However, the grid must still be fine enough that those solutions are not missed which might be confined to small regions in the parameter space. Furthermore, the number of neutrino paths from the Sun to the detector to cover the whole year of data recording was reduced compared to the pure two-flavour neutrino oscillations. This leads to slightly different χ^2-values for effectively pure two-flavour solutions, which are also found in the full analysis.

A subspaces of the entire possible parameter space have been investigated e.g. in [19] or [47]. In both publications an analytical expression for the survival propability $P^{(3)}_{e\to e}$ derived in [22] has been used, which is valid for large mass separations resp. small mixing angles. In this description $P^{(3)}_{e\to e}$ is determined by two 2-flavour probabilites $P^{(2)}_{e\to e}$ for each mass splitting Δm^2_{12} and Δm^2_{13}. By approximating the electron-density profile in the solar interior with an exponential function, $P^{(2)}_{e\to e}$ can also be evaluated analytically [22].

The results obtained in [19] or [47] could always been reproduced in the respective mass ranges. However, in those investigations of the three-flavour scenario, only the event-rate data were available. Using the new type of data (recoil-electron spectrum, zenith-angle and seasonal variations) almost all solutions found in [19,47] are disfavoured. Furthermore, new solutions are identifed since the respective parts of the parameter space were not covered in the analyses therein.

In the χ^2-analysis, applied to constrain the mixing parameters, always the whole available experimental data set was used for the present study. The Δm^2_{12}-Δm^2_{13}–plane is divided according to the two-flavour case in three subregions where the two oscillation-branches $\nu_1 \leftrightarrow \nu_2$ and $\nu_1 \leftrightarrow \nu_3$ are either both of matter type, or both of vacuum type, or one of matter and the second of vacuum nature.

1. Oscillations in the MSW mass regime

First sector I is investigated, where $\nu_1 \leftrightarrow \nu_2$ and $\nu_1 \leftrightarrow \nu_3$ both may undergo resonant MSW-transition, i.e. $10^{-9} \leq \Delta m^2_{12}, \Delta m^2_{13} \leq 10^{-3}\,\mathrm{eV}^2$. In Fig. 6 the projection of the region with $\chi^2 \leq 40$ on the 3-dimensional subspace Δm^2_{12}-Δm^2_{13}-$\sin^2 2\tilde{\Theta}_{13}$ is shown. The allowed parameters are located within the grey-shaded surroundings.

The pure two-flavour $\nu_1 \leftrightarrow \nu_3$ oscillations where the mixing into ν_2 is negligible are given by vertical structures. For instance, the LMA- and LOW-solutions are represented by the half-pillars at $\sin^2 2\tilde{\Theta}_{13} = 1$ and $\Delta m^2_{13} \approx 3.5 \times 10^{-5}$ and $10^{-7}\,\mathrm{eV}^2$. The horizontal planes provide the solutions independent of ν_3, and thus are two-flavour oscillations in the $1 \leftrightarrow 2$ system, where the influence from $\sin^2 2\Theta_{12}$ is not visible. However, the symmetry of sector I in the exchange of the indices 2 and 3 implies that they must be equivalent to solutions independent of ν_2. Therefore, the two planes around

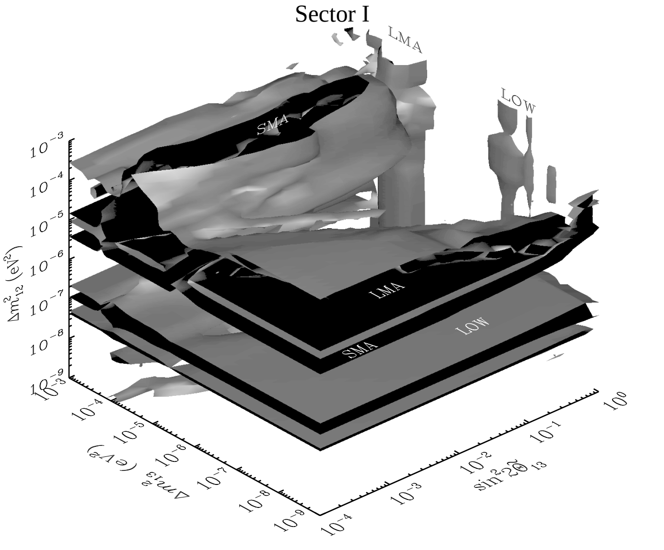

FIG. 6. Shaded volume representing the projection of the region with $\chi^2 \leq 40$ into the 3-dimensional subspace of Δm^2_{12}-Δm^2_{13}-$\sin^2 2\tilde{\Theta}_{13}$ for MSW-transitions in the $\nu_1 \leftrightarrow \nu_2$ and $\nu_1 \leftrightarrow \nu_3$ system (sector I). The allowed values are located within the light shaded surroundings. The position of the classical two-flavour solutions are also shown, which may be located in the $1 \leftrightarrow 2$ as well as in the $1 \leftrightarrow 3$ system.

$\Delta m^2_{12} \approx 10^{-7}\,\mathrm{eV}^2$ are equivalent to the pillar-like structures at $\sin^2 2\tilde{\Theta}_{13} = 1$ and $\Delta m^2_{13} \approx 10^{-7}\,\mathrm{eV}^2$ and can thus be identified as two representations of the LOW-solution. Similarly the planes at $\Delta m^2_{12} \approx 10^{-4}\,\mathrm{eV}^2$ are LMA- (upper) and SMA- (lower plane) solutions. The three-flavour solutions with the smallest χ^2-values are sited near the intersection regions of the horizontal planes and vertical objects, which means that they are at least slightly more probable than the pure two-flavour solu-

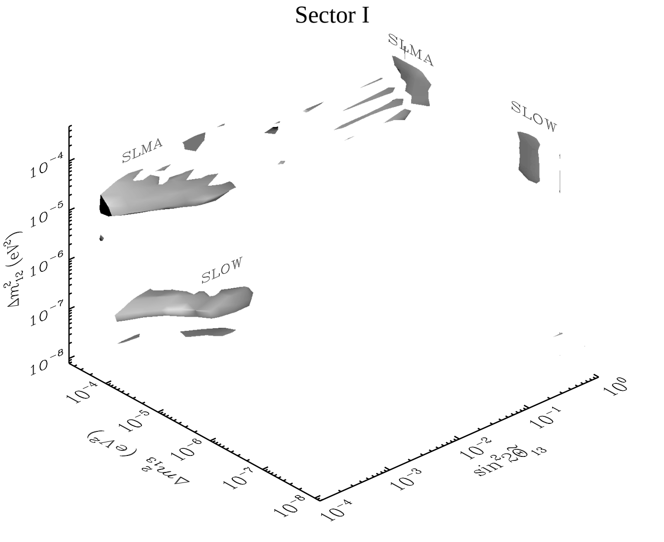

FIG. 7. Zoom into the shaded volume of Fig. 6 showing the position of the SLMA- and SLOW-solutions. The shaded bodies enclose the regions with $\chi^2 \leq 34.3$.

tions and involve indeed all three flavours.

In Fig. 7 the regions with $\chi^2 \leq 34.3$ of the present survey are shown. Due to the symmetry in $\nu_2 \leftrightarrow \nu_3$ the four basic regions in this figure belong only to two distinct solutions. They can be identified as combinations of a SMA-solution in $\nu_1 \leftrightarrow \nu_3$ ($10^{-4} \lesssim \sin^2 2\tilde{\Theta}_{13} \lesssim 10^{-3}$) and a LMA resp. LOW in $\nu_1 \leftrightarrow \nu_2$ ($\Delta m^2_{12} \approx 10^{-5}$ and $10^{-7}\,\mathrm{eV}^2$), therefore denoted SLMA and SLOW. The assignment of $\nu_1 \leftrightarrow \nu_3$ to SMA and $\nu_1 \leftrightarrow \nu_2$ to LMA resp. LOW is ambiguous and could also be chosen vice versa. This is reflected by the second appearance of the SLOW- and SLMA-solutions in Fig. 7 at $\sin^2 2\tilde{\Theta}_{13} \approx 1$ and $\Delta m^2_{13} \approx 10^{-7}$ and $10^{-5}\,\mathrm{eV}^2$.

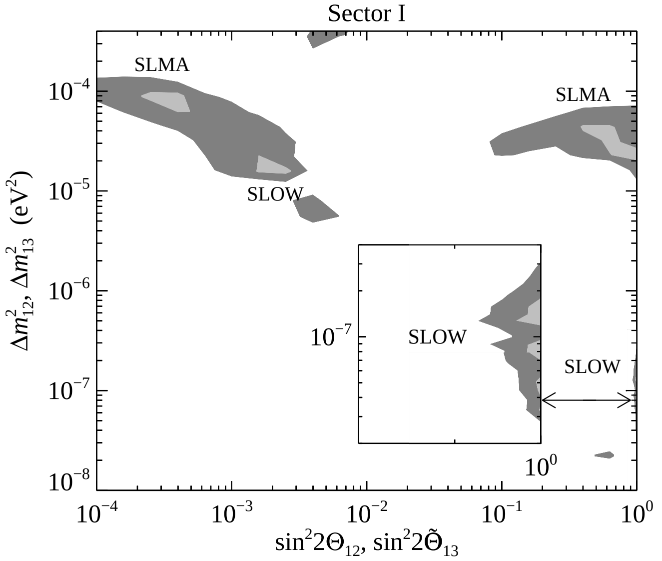

FIG. 8. Projection of the SLOW and SLMA-solutions onto the Δm^2_{12}-$\sin^2 2\Theta_{12}$– or the Δm^2_{13}-$\sin^2 2\tilde{\Theta}_{13}$–plane. The dark and bright shaded areas show the regions of $\chi^2 \leq 34.3$ and $\chi^2 \leq 32.3$. Following the assignment of Table IV, the 2σ-region of the SLMA- and SLOW-solution merge in the projection onto the Δm^2_{13}-$\sin^2 2\tilde{\Theta}_{13}$–plane, but are well separated in the Δm^2_{12}-$\sin^2 2\Theta_{12}$–plane (see also Fig. 7).

In Fig. 8 the projection of the SLMA- and SLOW-solutions into the typical two-flavour planes are shown. One of the areas labelled SLMA (SLOW) has to be identified with oscillations in $\nu_1 \leftrightarrow \nu_2$ and the other with ν_1-ν_3–mixing. The oscillation parameters are provided in Table IV together with the χ^2-values. Since two more parameters are adjusted in the three-neutrino as compared to the two-neutrino case, the number of degrees-of-freedom reduces from 24 to 22.

The mixing angle of the small mixing-angle branch in the SLMA-solution is about one order of magnitude smaller than the usual SMA-solution (compare Figs. 8 and 4). With the χ^2-"valley" of the SLMA-solution extending to even smaller mixing angles the pure LMA-solution is included in this confidence region. Thus, the SLMA-solution can be characterized by an LMA-solution with a tiny contribution of small-angle mixing into the third neutrino flavour. The good agreement of the zenith-angle dependence of the SLMA-solution with the data as shown in Fig 13 supports this assessment (see also Table IV). The small SMA-contribution of the third flavour to the LMA-solution improves the fit with the energy-bin data of Super-Kamiokande. By way of contrast, in the SLOW-solution it cannot be figured out, whether SMA or LOW is the dominant portion.

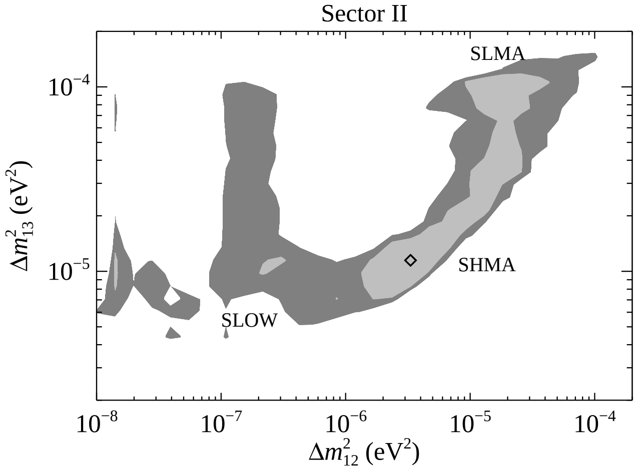

FIG. 9. Projection of the SHMA-solution in sector II onto the Δm^2_{13}-Δm^2_{12}–plane. The χ^2-levels of the regions agree with those of Fig. 8. The best fit value is marked by $\diamond$. The tiny-92.8% C.L.-region (light shaded) at $\Delta m^2_{12} = 1.4 \times 10^{-8}\,\mathrm{eV}^2$ reflects a second SLOW-solution with almost the same χ^2-values as the usual SLOW-solution found in sector I (Fig. 8).

In addition to the solutions found in sector I of the flavour space (Fig. 2), I could also identify a solution in sector II, where $\pi/4 \leq \sin\Theta_{12} \leq \pi/2$ and $\tan\Theta_{13} \leq \sin\Theta_{12}$. In Figs. 9 and 10 the projections of this solution, in the following called SHMA ("small and huge mixing angle"), into various planes are shown. Note, that unlike in the SLMA- or SLOW-solution, ν_2 and ν_3 cannot be exchanged in SHMA, as sector II is not invariant under this transformation.

Since the best fit values of the SLMA- and SLOW-solutions are obtained for $\sin^2 2\Theta_{12} = 1$ ($\Theta_{12} = \pi/4$), these solutions are also apparent in sector II, as at this angle sector I and II meet. In Fig. 10 these parts of the confidence areas of the SLMA- and SLOW-solutions are visible for which $\Theta_{12} \geq \pi/4$. While SLOW and SLMA seem to be distinct solutions in sector I, it appears, that both are "foothills" of a common deeper minima (SHMA) in sector II. In the projection onto the Δm^2_{13}-$\sin^2 2\tilde{\Theta}_{13}$–plane the confidence region of the SLMA-, SHMA- and SLOW-solution merge, which is expected, as already the SLOW- and SLMA-confidence region merged in this projection of sector I (cf. Fig. 8).

The SHMA-solution has a small mixing-angle portion in the ν_1-ν_3–branch with almost the same mixing parameters like the SLOW-solution (Table IV). The squared-mass difference in $\nu_1 \leftrightarrow \nu_2$ resembles the SLMA-solution.

TABLE IV. The most favoured solutions within the three-flavour oscillation scenario and the respective χ^2-values. The second column indicates the sector in the flavour space, where the solution has been found (see also Fig. 2). Δm^2_{ij} is in units of eV^2 and s^2_{ij} abbreviates here $\sin^2 2\Theta_{ij}$. In sector I $\sin^2 2\tilde{\Theta}_{13}$ is defined by Eq. (13), analogously in sector II by Eq. (14). χ^2_R, χ^2_e, χ^2_Z and χ^2_A are the individual contributions to χ^2_{tot} as defined by Eqs. (15)–(17). The number of d.o.f. is 22.

		Δm^2_{12}	s^2_{12}	Δm^2_{13}	$\tilde{s}_{13}$	χ^2_R	χ^2_e	χ^2_Z	χ^2_A	χ^2_{tot}
SLOW	I	8.0×10^{-8}	1.00	1.4×10^{-5}	2.1×10^{-3}	0.52	23.5	7.0	0.2	31.2
SLMA	I	1.9×10^{-5}	1.00	1.0×10^{-4}	2.2×10^{-4}	2.94	23.6	4.0	1.4	31.9
SHMA	II	3.3×10^{-6}	0.64	1.1×10^{-5}	3.7×10^{-3}	0.82	24.2	2.6	1.5	29.0
VO 3	I	5.5×10^{-11}	0.62	2.6×10^{-10}	0.60	2.13	18.2	8.6	1.5	30.4
VO 3'	II	4.5×10^{-11}	0.63	3.0×10^{-10}	0.68	2.43	19.7	8.6	1.3	32.1
SVO	I	4.4×10^{-10}	0.82	1.7×10^{-5}	1.6×10^{-3}	1.46	17.2	8.4	1.5	28.6

Since $\Theta_{12} \geq \pi/4$ the ν_1-ν_2–mixing contributes a ν_e-suppression, which is only weakly energy-dependent (illustrated e.g. in Fig. 1 for $\sin^2 2\Theta = 0.7$). But actually it is this slight energy dependence which enables to constrain the squared-mass difference of Δm^2_{12}. In the projection of sector II onto the Δm^2_{12}-Δm^2_{13}–plane (Fig. 9), the dependence of the solution on a predefined value for Δm^2_{13} or Δm^2_{12} is visible. If, for instance, Δm^2_{13} is fixed to be $10^{-4}\,\mathrm{eV}^2$, Δm^2_{12} has to be increased, favoring in this case the SLMA-solution.

Like the SLMA- and SLOW-solutions, SHMA can neither reproduce the recoil-electron spectrum of Super-Kamiokande satisfactorily (cf. Fig. 13(a) and Table IV). However, by the SHMA-solution the best fit of all solutions presented in this work to the zenith-angle variation is obtained. In particular, also the slightly enhanced first night-bin ($-0.2 \leq \cos\zeta \leq 0$) can be reproduced by this solution (Fig. 13(b)).

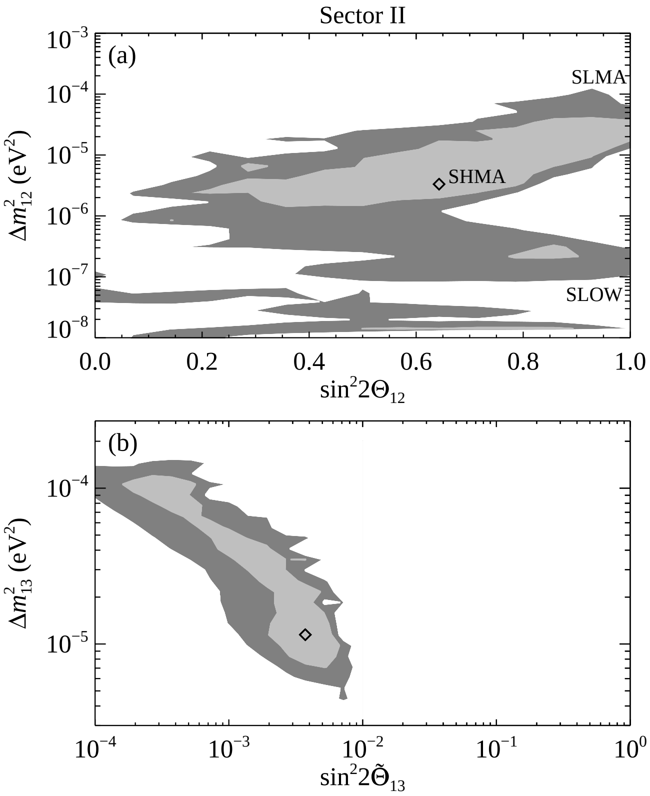

FIG. 10. Projection of the SHMA-solution in sector II onto the Δm^2_{12}-$\sin^2 2\Theta_{12}$– resp. Δm^2_{13}-$\sin^2 2\tilde{\Theta}_{13}$–plane. The χ^2-levels of the regions agree with those of Fig. 8. The best-fit value is marked by $\diamond$.

2. Three-flavour vacuum oscillations

In the case when both squared-mass differences are in the vacuum-oscillation regime (Δm^2_{12},$\Delta m^2_{13} \leq 10^{-9}\,\mathrm{eV}^2$) two minima could be found, denoted VO 3 and VO 3'. While VO 3 is located in sector I (Fig. 11), i.e. $0 \leq \Theta_{12} \leq \pi/4$, VO 3' has been found in sector II (Fig. 12), where $\pi/4 < \Theta_{12} \leq \pi/2$. Thus although they seem to have very similar mixing parameters (Table IV), there are really distinct solutions with different properties. For instance, the predicted recoil-electron spectrum of VO 3' shows an oscillating variation with energy, which is not

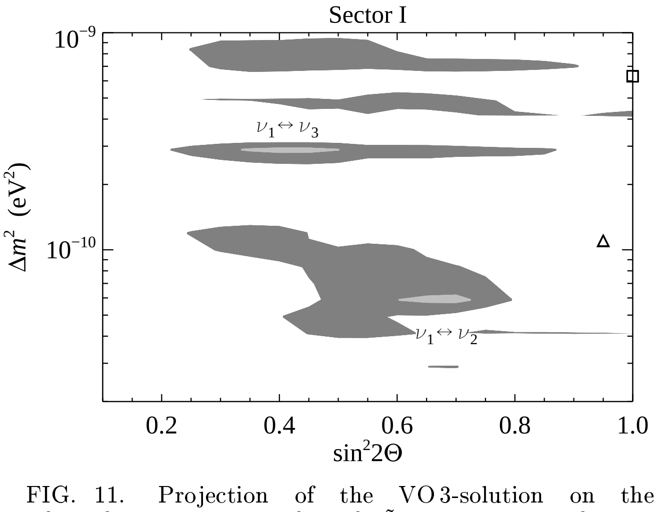

FIG. 11. Projection of the VO 3-solution on the Δm^2_{12}-$\sin^2 2\Theta_{12}$– resp. Δm^2_{13}-$\sin^2 2\tilde{\Theta}_{13}$–plane. The χ^2-levels of the regions agree with those of Fig. 8. The best-fit value of the two-flavour VO-solution reproducing solely the event rates is marked by $\triangle$, while the position of the two-flavour VO-solution in the complete analysis is shown by $\square$.

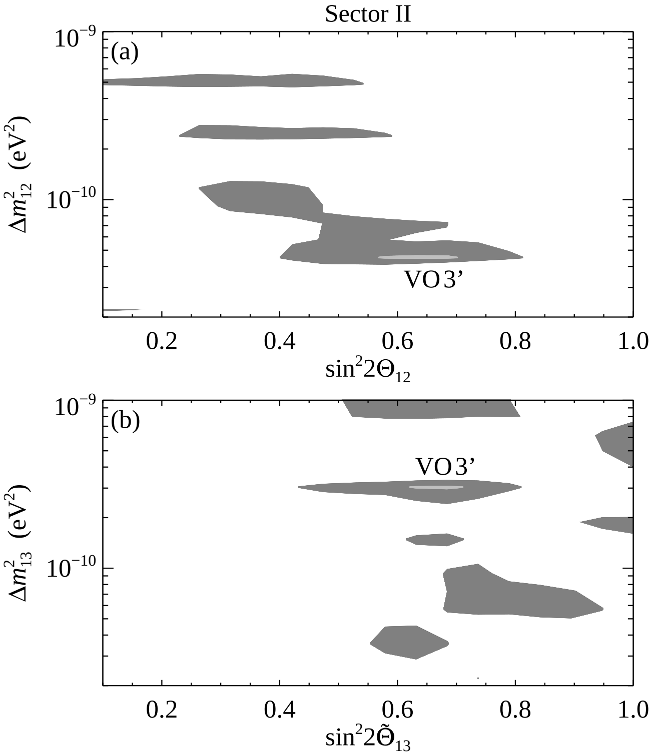

FIG. 12. Projection of the VO 3'-solution on the Δm^2_{12}-$\sin^2 2\Theta_{12}$– and Δm^2_{13}-$\sin^2 2\tilde{\Theta}_{13}$–plane. The χ^2-levels of the regions agree with those of Fig. 11.

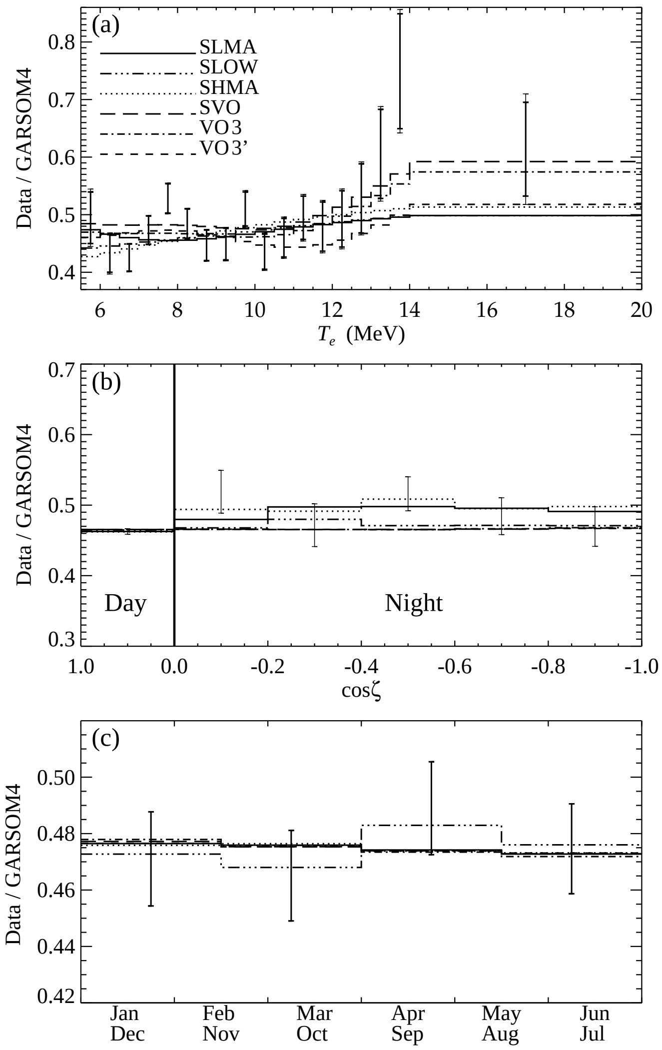

FIG. 13. Recoil-electron spectrum (a) zenith-angle (ζ) variation (b) and seasonal dependence (c) of the best fit three-flavour solutions including all available solar neutrino data compared with the measurements of Super-Kamiokande. The experimental data agree with Fig. 5.

visible for VO 3 (Fig. 13). The minimal χ^2-values for VO 3 and VO 3' are similar to the SLOW- and SLMA-solutions slightly favoring VO 3 (Table IV). With these 3-flavour vacuum solutions the recoil-electron energy spectrum could be reproduced almost as well as with the 2-flavour VO-solution (Fig. 13), and additionally the event rates agree fairly well with the measured rates of the solar-neutrino detectors. The VO 3- and VO 3'-solutions show a compromise between the VO-solution (triangle in Fig. 11) obtained by fitting solely the event-rate data and the VO-solution of the complete analysis (□ in same figure). The mixing angles for the 3-flavour vacuum solution are only about one half of the usual 2-flavour VO-solution, as ν_e is now oscillating nearly equally strong into *two* other flavours.

3. Mixed vacuum and MSW oscillations

The combination of oscillation between two neutrino flavours in the MSW mass-regime and an additional vacuum oscillation into the third flavour is investigated completing the mass ranges which have not been covered by the previous sections. This case has been examined in [47] for $10^{-7} \le \Delta m^2_{13} \le 10^{-4}\mathrm{eV}^2$ and $10^{-12} \le \Delta m^2_{12} \le 10^{-9}\,\mathrm{eV}^2$. However, in that analysis only the event rates have been included, but not the recoil-electron spectrum, the zenith-angle dependence nor the annual variation data recorded by Super-Kamiokande. Furthermore, the Earth-regeneration effect has been neglected. Therefore, this case is reinvestigated including all the available data and calculating the electron-neutrino survival probabilities fully consistently including the Earth effect like in the previous sections.

In this survey Δm^2_{13} is taken to be in the mass range of the MSW-solution ($10^{-9} \le \Delta m^2_{13} \le 10^{-3}\,\mathrm{eV}^2$) and Δm^2_{12} in the vacuum oscillation area ($10^{-12} \le \Delta m^2_{12} \le 10^{-9}\,\mathrm{eV}^2$). With these conventions about Δm^2_{13}, two possibilities are conceivable for the $\nu_1 \leftrightarrow \nu_3$ system, a resonant and a non-resonant oscillation. Since the masses are well separated, the condition for a resonance obtained in the two-flavour case can be applied (Eq. 11)

$$N_{\mathrm{res}} = \frac{\Delta m^2_{13}/2E}{\sqrt{2}G_{\mathrm{F}}}\cos 2\Theta_{13} > 0.$$

Thus, an MSW flavour transition is only possible, if the mixing angle Θ_{13} is less than $\pi/4$. In the $\nu_1 \leftrightarrow \nu_2$ system only pure vacuum oscillations occur, and thus $\Theta_{12} \leq \pi/4$. Since the solution may be a combination of a vacuum oscillation in the $1 \leftrightarrow 2$ and a resonant resp. non-resonant oscillation in the $1 \leftrightarrow 3$ branch, the complete essential parameter space for $10^{-9} \leq \Delta m^2_{13} \leq 10^{-3}\,\mathrm{eV}^2$ and $10^{-12} \leq \Delta m^2_{12} \leq 10^{-9}\,\mathrm{eV}^2$ is therefore covered by $\Theta_{12} \leq \pi/4$ and $\Theta_{13} \leq \pi/2$.

Basically one minima could be found in the parameter space of this subsurvey, which is a combination of a SMA-solution in the $\nu_1 \leftrightarrow \nu_3$ ($\Theta_{13} \leq \pi/4$) and an additional VO-mixing in $\nu_1 \leftrightarrow \nu_2$, therefore denoted SVO. This solution is similar to the solution "C" found in [47].

In a second computation the parameter region around the SVO-solution has been analyzed in greater detail. The projections of the derived confidence levels onto the Δm^2_{13}-$\sin^2 2\Theta_{13}$– and Δm^2_{12}-$\sin^2 2\Theta_{12}$–plane are shown in Fig. 14. From the complete scan it can be inferred that no further minima are obtained for $\sin^2 2\Theta_{13} \leq 10^{-3}$ and that the region with $\chi^2 \leq 34.3$ extends at most down to $\sin^2 2\Theta_{13} = 10^{-4}$. For smaller mixing angles the SVO-solution merges with the two-flavour VO-solution which, in contrast to the SVO-solution, poorly fits the event rates (see Tables III and IV).

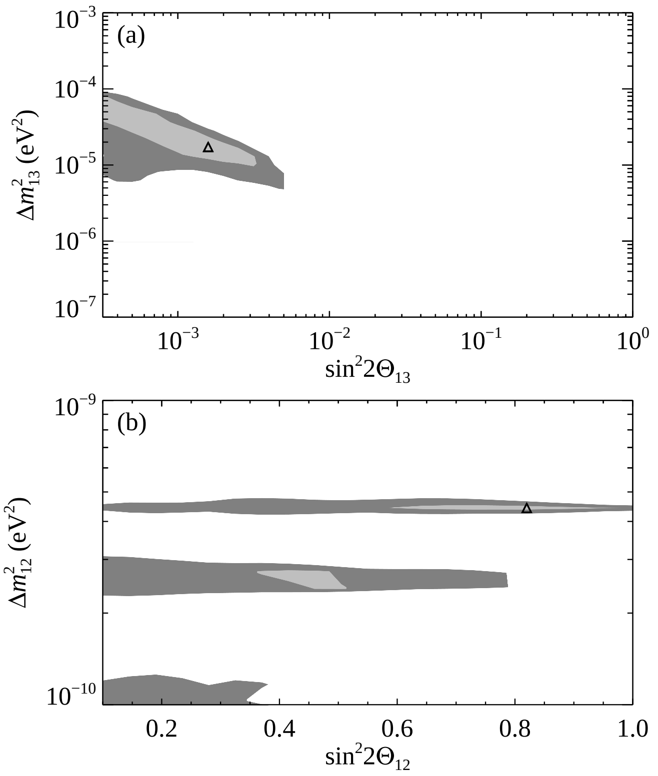

FIG. 14. Projections of the SVO-solution onto the Δm^2_{12}-$\sin^2 2\Theta_{12}$– and Δm^2_{13}-$\sin^2 2\Theta_{13}$–plane obtained from a detailed survey especially around the SVO-area. To show the position and shape of this solution the χ^2-levels are chosen to be 30.8 (bright) and 34.3 (dark shaded). The triangles marks the best-fit value of this solution. ($\Theta_{12}, \Theta_{13} \leq \pi/4$)

The SVO- and the SHMA-solution are presently the favored three-flavour solutions to the solar neutrino problem. The SVO-solution combines the merit of the VO-solution to explain the recoil-electron spectrum (Fig. 5) and the property of the SMA-solution to reproduce the event rates (Table III). Like in the SLOW-solution it is difficult to make any statement into which direction the SVO-and SHMA-solution may develop, when the statistics in forthcoming data is going to improve. Will they remain real three-flavour solutions, or will they merge with their respective two-flavour solution-portions?

V. PROSPECTS FOR FUTURE EXPERIMENTS

Future neutrino experiments like SNO or Borexino will provide further information to determine the correct solution to the solar neutrino problem. In the following the ability of these detectors to discriminate the various two- and three-flavour solutions will be discussed.

A. Borexino

In Fig. 15(a) the expected recoil-electron spectrum in Borexino of the two- and three-flavour solutions is shown. The hatched areas indicate the uncertainties in the mixing parameters of the SMA- and LMA-solutions. These areas were obtained by allowing the mixing parameters to vary within the 2σ confidence region of the Δm^2-$\sin^2 2\Theta$–plane (see Fig. 4). For the LOW-solution no region is applied, as this solution appeared only within the 3σ level.

While in the presently operating detectors, the ^{7}Be-neutrinos contribute, if at all, only a small portion to the total event rate, Borexino is going to measure almost solely these neutrinos. In the case of the SMA-solution it should detect only about 25% of the event rate as predicted by GARSOM4, while in the LMA-case about 65% are expected (Fig. 15(a)). Actually, for the SMA-solution the rate is basically due to the interaction of the ν_μ (or ν_τ) with the detector, as in this solution the ^{7}Be-neutrinos almost totally consist of ν_μ-flavour. This leads to an unmistakable signal of the SMA compared to the LMA-solution: An excess in the lowest energy bin of up to 50% compared to the other bins. Thus, with good statistics in the low energy bins SMA could be clearly distinguished from LMA in Borexino.

One of the main advantages of this detector is the ability to monitor seasonal variations in the neutrino signal — the vacuum survival probability is modified by the eccentric orbit of the Earth (Eq. 10). Since the ^{7}Be-neutrinos are unlike ^{8}B-neutrinos emitted to 90% in a monoenergetic line at 0.862 MeV the signal in the detector is not smeared out like in Super-Kamiokande. A detailed analysis about the sensitivity of Borexino to detect vacuum oscillations is given in [48].

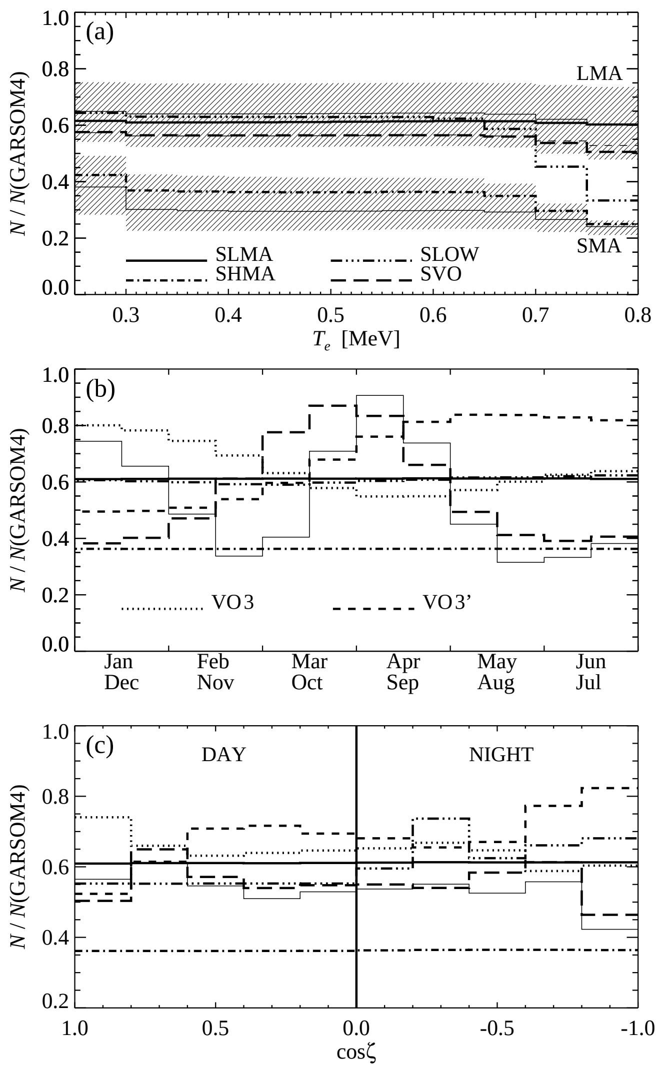

FIG. 15. Expected recoil-electron spectrum in Borexino for the best-fit three-flavour solutions. In (a) only the solutions undergoing an MSW-transition are shown; the vacuum solutions can be identified by a seasonal variation as plotted in (b). The hashed area in (a) is obtained by allowing the mixing parameters to vary within the 2σ-range of the two-flavour LMA resp. SMA-solution shown in Fig. 4. The thin lines represent the best-fit two-flavour solutions (solid line in (a): SMA resp. LMA, dashed line in (a); LOW, solid line in (b) and (c): VO). In the seasonal variation (c) the flux changes due to the eccentricity of the Earth's orbit have been subtracted.

The sensitivity of the ^{7}Be-neutrino flux in the VO-regime is also visible in the zenith-angle dependence of the event rate in Borexino (Fig. 15(c)). In particular, the rates of those zenith angles, under which the Sun appears only around the winter or summer solstice ($|\cos\zeta| \gtrsim 0.6$), are influenced by the modulation of the ^{7}Be-neutrino signal with the Sun-Earth distance. Note that unlike the Earth regeneration effect, which in the MSW mass-range can lead to a variation of the event rate with the zenith angle only during the night, for VO-solutions a variation in the signal over the whole day is apparent. The magnitude of the zenith-angle variation however is smaller, as each zenith-angle bin is an average over many positions of the Earth in its solar orbit. Therefore, the seasonal variation of the event rates are more sensitive to detect VO-solutions as the zenith-angle dependence. For the best-fit mixing parameters of the MSW-solutions SMA, LMA and LOW, no Earth regeneration takes place for the energy of the ^{7}Be-neutrinos, and thus no zenith-angle variation of the event rates in Borexino is expected for these cases.

The expected recoil-electron spectrum and annual variation in Borexino for the best-fit values of the three-flavour solutions SLMA, SLOW, SHMA, SVO, VO 3 and VO 3' are shown in Fig. 15, too. As already described above, the SLMA is very similar to the LMA-solution and therefore also difficult to disentangle from the latter in the Borexino data. The SLOW-solution leads to a clear signature in Borexino compared to the two-flavour solutions. It has a strongly reduced event rate in the high-energy bins of Borexino, which are not observed in any of the 2-flavour solutions.

Both 3-flavour vacuum oscillations show a very similar signal in all data of Borexino (energy, zenith-angle and season) and thus, they can hardly be disentangled. For this reason and to avoid additional confusion, both solutions are denoted in the following, if not explicitly mentioned, by VO 3.

The properties of VO 3 are very sensitive to the exact mixing parameters. Even very small variations can produce a recoil-electron spectrum which resembles those of the SHMA-, SVO- or SLOW-solutions. However the seasonal dependence of the signal can be used to discriminate between VO 3 and SLOW resp. SHMA. VO 3 shows a strong annual dependence, which is not present in the SLOW- or SHMA-solution. Furthermore, the SLOW-solution leads to a zenith-angle dependent signal due to the Earth regeneration effect (Fig. 15(c)). The VO 3- and SVO-solutions also have a zenith-angle dependence, but the reason for this lies in the seasonal modulation of the event rates in these solutions. Thus, for the VO 3- and SVO-solutions also a zenith-angle variation during the day are expected.

The identification of the SVO-solution is more difficult, since only a weak depletion of the high-energy bins is predicted, which may not be detectable. The annual variation of the SVO-signal stems from the vacuum-oscillation branch of the solution. Since the VO 3-solution is very sensitive to the exact mixing parameters it cannot be excluded that the same annual variation is obtained for SVO and a three-flavour vacuum solution. A pure two-flavour vacuum oscillation with $\Delta m^2 = 4.4 \times 10^{-10}\,\mathrm{eV}^2$ and $\sin^2 2\Theta = 0.82$ causes a similar seasonal dependence of the event rate in Borexino like SVO. However, such a solution would produce 4.2 SNU in the Homestake experiment, which is about 60% higher than the recorded rate. Thus, measuring a annual variation of the signal in Borexino peaked around the beginning of spring resp. of autumn and almost equally low at the summer and winter solstices would at least provide a strong hint, that the solution to the solar neutrino problem is rather a three-flavour SVO- or VO 3-solution than a pure two-flavour VO-solution.

B. SNO

Recently, SNO has started to measure solar neutrinos in the same energy window as Super-Kamiokande, however with a better energy resolution and the ability to discriminate the CC- and NC-events. Since the total number of neutrinos does not change by neutrino oscillations (only their flavour), the number of NC-events has to agree with the no-oscillation scenario, i.e. the total number of solar neutrinos independent of their flavour can be determined by this quantity‡. Therefore, no departures in the recoil-deuterium energy spectrum, zenith-angle or seasonal dependence from the standard (no-oscillation) values are expected for NC-events. The merit of SNO is the measurement of the ratio of CC- to NC-events, as with this quantity the ν_e-contribution to the total solar neutrino flux is connected. A measured CC/NC-ratio smaller than the standard one unambiguously proves that the solar neutrinos, initially ν_e's, are oscillating into another flavour during their flight from the solar interior to the Earth.

If the excess in the high-energy bins of Super-Kamiokande is confirmed by continuing measurements, the CC/NC-ratio in SNO will enable to discriminate between an explanation by neutrino oscillations and by an enhanced *hep*-neutrino flux, which currently is also under discussion [18]. While for the latter solution the *hep*-neutrinos would equally contribute to the CC- and NC-events leading to a constant CC/NC-ratio, for the oscillation scenario a similar excess like in Super-Kamiokande would be also apparent in the CC/NC-ratio of SNO.

To illustrate the expectations for the deuterium-recoil spectrum and zenith-angle dependence of the CC-events in SNO, the first and second moments of these distributions are calculated (for definition see [13]). The first moment provides the mean value and the second a measure of the width of the distribution.

With very small annual or daily changes in the Super-Kamiokande detector, such variations are neither expected for CC-events (e-ν_e–scattering) in SNO. Thus, for the zenith-angle moments in SNO only small deviations from the standard value are predicted for the two-flavour SMA-, LMA- and LOW-solution (Fig. 16(b)).

The error bars for these solutions in Fig. 16 were obtained in the same manner as for the recoil-electron spectrum in Borexino. Since the best-fit values are not very

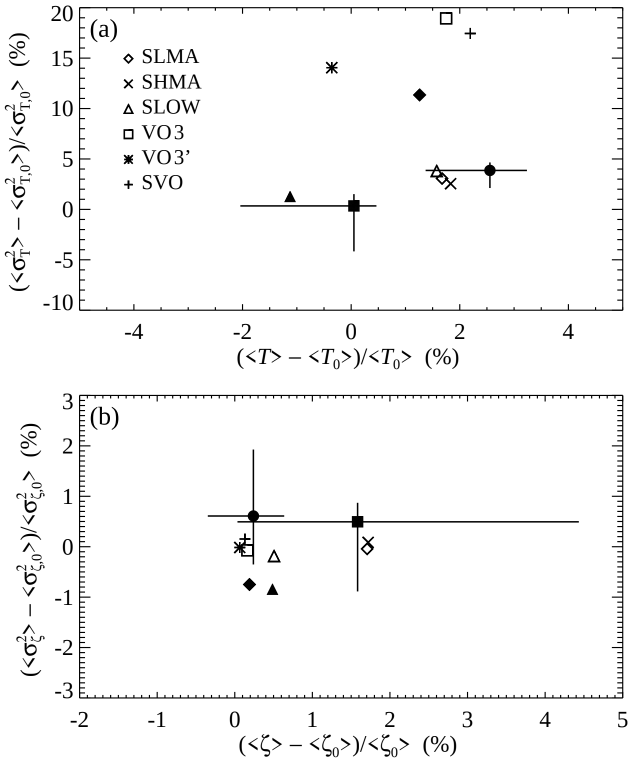

FIG. 16. Predicted values for the moments of the recoil-deuterium spectrum (upper panel) and the zenith angle moments (lower panel) for CC-events in SNO in case of the three-flavour solutions. The filled symbols represent the two-flavour solutions LMA (■), SMA (•), LOW (▲) and VO (♦) of Fig. 4. The error bars were obtained in the same manner as the hashed area in Fig. 15(a).

well separated in the plane of the first two zenith-angle moments, it seems to be very difficult to disentangle the SMA-, LMA- and LOW-solution by forthcoming zenith-angle data of SNO. A similar behaviour is expected for the moments of the recoil-deuterium energy spectrum [49] shown in Fig. 16(a). However, since the energy resolution in SNO is better than in Super-Kamiokande (Table V) more significant data can be expected to disentangle the true solution to the solar neutrino problem. A more detailed discussion about the properties of SNO to discriminate the 2-flavour solutions can be found in [50].

As further illustrated in Fig. 16 SNO appears to be able to discriminate LMA- and SLMA-solution, as the latter distorts the recoil-deuterium moments like SMA, but the zenith-angle moments like LMA. However, since the separation of SLMA and SMA in the first zenith-angle moment is only about 1-2% and even less in the second moment, good statistics is needed to disentangle these solutions. For SLOW the situation is worse to be identified by SNO, as this solution produces very similar signals like the SMA-solution.

For pure two-flavour vacuum oscillations presently no reasonable favored parameter range can be obtained.

‡ Provided, no mixing with sterile neutrinos occurs.

Therefore, it is not possible to decide, whether a strong deviation of the recoil-deuterium spectrum resp. of the zenith-angle moment from the standard value is due to a three-flavour oscillation of SVO resp. VO 3-type or due to a pure two-flavour vacuum oscillations. Improved statistics in Super-Kamiokande and forthcoming results from Borexino and SNO are needed to enable a clear discrimination between all the various presently allowed two- and three-flavour oscillation solutions.

VI. DISCUSSION

The most favored solutions to the solar neutrino problem in the scope of two- and three-flavour neutrino oscillations have been investigated in this work. For this purpose the evolution of the neutrino state was followed numerically from the solar interior, where the neutrinos are produced in the fusion reactions, through Sun, space and Earth to the neutrino detectors without falling back to analytical approximations (cf. Appendix).

Six new solutions in the three-flavour case could be found, among which SHMA and SVO are at least as probable as the presently favored two-flavour LMA-solution. The SLMA-, SLOW-, VO 3 and VO 3'-solutions, with which the measured event rates, recoil-electron spectrum, zenith-angle dependence and annual variation are reproduced slightly worse than with SHMA or SVO, are nevertheless still good candidates as solution to the solar neutrino problem. The new experiments Borexino and SNO, which recently has started to operate, and improved statistics in Super-Kamiokande will partly enable to discriminate the various two- and three-flavour solutions. Basically, with Borexino the vacuum-oscillation solutions will leave a clear footprint in the annual variation of the event rates, with which they can be distinguished from MSW-solutions. Additionally, in case of the SLOW-solution the high energy bins of the recoil-electron energy spectrum will be significantly depleted compared to the other energy bins and a day-night asymmetry of about 10% is expected, which is not predicted for any other solution.

In this work it was investigated whether the poor fits of two-flavour neutrino oscillations to the solar neutrino data can be improved by including all three flavours. But the three-flavour case cannot be examined totally independent of the results obtained for the atmospheric neutrinos. The most promising solution to the atmospheric neutrino problem is presently the oscillation between ν_μ and ν_τ with a squared-mass difference $\Delta m^2_{23} \approx 10^{-3}\,\mathrm{eV}^2$ [51]. This demands that the sum or difference of Δm^2_{12} and Δm^2_{13} is equal to Δm^2_{23}. However, none of the presented three-flavour solutions fulfills this condition, which implies that either the three-flavour solutions SLMA, SHMA, SLOW, VO 3, VO 3' and SVO are excluded or that the origin of the atmospheric neutrino problem are not ν_μ-ν_τ–oscillations.

Including three-flavour neutrino oscillations it has been found that with $\Delta m^2_{23} \approx 10^{-4}\,\mathrm{eV}^2$ solutions to the atmospheric neutrino deficit exist, if Δm^2_{12} is of the order of the LMA-solution and $\sin^2 2\Theta_{13} \gtrsim 10^{-2}$ [52]. While the squared-mass differences would be consistent with the SLMA-solution ($\Delta m^2_{12} = 1.9 \times 10^{-5}$ and $\Delta m^2_{13} = 10^{-4}\,\mathrm{eV}^2$), $\sin^2 2\Theta_{13}$ of SLMA is only about 10^{-4} and thus two orders of magnitude smaller than demanded in [52].

In the two-flavour solutions LMA, SMA, LOW and VO it is implicitly assumed that the mixing into the third flavour is negligible. Thus, these solutions are not coupled to the atmospheric neutrino problem, as they can easily be taken as ν_e-ν_μ–oscillations, where no mixing between ν_e and ν_τ appears. If however the results of the LSND-collaboration [53], which claimed to have detected ν_e-ν_μ–oscillations with $\Delta m^2_{12} \gtrsim 10^{-2}\,\mathrm{eV}^2$, are confirmed by KARMEN2 [54], it will be difficult to solve the solar and atmospheric neutrino anomaly simultaneously by the oscillation of three neutrino flavours. A four-neutrino scheme has been proposed (one sterile and three active neutrinos) to cover the three different mass scales involved by the LSND-result, atmospheric and solar neutrino problems [55]. In any case, identifying the solution to the solar neutrino puzzle by future data of forthcoming and presently operating solar-neutrino detectors may also constrain the solutions for the atmospheric neutrino problem or vice versa.

The possibility that two-flavour neutrino oscillations are responsible for the solar neutrino puzzle appears to be supported by the relatively weak improvement of the fit by increasing the parameter space from 2 (two flavours) to 4 dimensions (three flavours). Almost all three-flavour solutions found are combinations of 2 two-flavour solutions, where each of it is able to explain a certain type of data set. However, nearly all two-flavour solutions reproduce at most two of the four kind of data at once, the annual variation and then either the rates (SMA), the recoil-electron energy spectrum (VO) or the zenith-angle dependence (LOW). Three-flavour solutions composed of these solutions still fail to reproduce one type of data set, e.g. the SVO-solution cannot explain the zenith-angle modulations of the event rates.

Among the two-flavour solutions only LMA reliably reproduces all kind of data apart from the recoil-electron spectrum. As no combination of the LMA-solution with a second solution could be found with which the fit could be improved considerably, this may be a hint, that the errors in the energy bins are greater than assumed, or that perhaps unknown systematic errors are apparent [18]. A reason for the bad fit of all solutions to the data may also be, that in the analysis performed in this work, possible correlations between the different type of data sets in Super-Kamiokande have been neglected, as they are not available. Including such correlations may reduce the χ^2-values, which could improve the fit to an acceptable level.

Removing the contribution of the recoil-electron spectrum and including the results of the atmospheric neutrino data, i.e. $\Delta m^2_{23} \approx 10^{-3}\,\mathrm{eV}^2$, favors the LMA-solution, which implies that no mixing between ν_1 and ν_3 occurs ($\Theta_{23} = 0$). If the explanation of the atmospheric neutrino deficit, however, is found not to be neutrino oscillations, three-flavour oscillations are allowed in any mass range, implying that the SHMA-solution leads to the best fit to the data.

Finally, I would like to remark, that the slightly better fit of the SVO-solution in comparison with the LMA-solution is basically because of the excess in the high-energy bins of the recoil-electron spectrum of Super-Kamiokande. This excess, however, has been more pronounced in the data of the first 504 days [14] yielding a higher probability for the SVO-solution than with the 708-days data. It may well be that it totally disappears in forthcoming data and two-flavour solutions reproduce the spectrum convincingly. Apart from the questionable LSND-results, the atmospheric as well as the solar neutrino problem can then be well solved independently by neutrino oscillations.

ACKNOWLEDGMENTS

I am grateful to Achim Weiss and Wolfgang Hillebrandt for their inspiring comments and suggestions. Furthermore, the support of Georg Raffelt in particle-physics questions is acknowledged. I also want to thank Jørgen Christensen-Dalsgaard for his help in further improving the solar model. Moreover, I am thankful to Sarbani Basu for providing me the seismic model, to Scilla Degl'Innocenti for the seismic error data, to John N. Bahcall for the detector response functions and other useful quantities of SNO and to Lothar Oberauer for the data about the Borexino properties. This work was supported by the "Sonderforschungsbereich 375-95 für Astroteilchenphysik" der Deutschen Forschungsgemeinschaft.

APPENDIX: FROM THE INITIAL NEUTRINO STATE TO THE EVENT RATES

To obtain event rates for the various detectors a variety of averages and integrals have to be evaluated. In this section briefly a numerical scheme is described, how accurate predictions for the event rates can be calculated numerically.

For a certain set of parameters Δm^2_{12}, Δm^2_{13}, $\sin^2 2\Theta_{12}$ and $\sin^2 2\Theta_{13}$ the evolution of an initially pure electron-neutrino from the solar interior to the terrestrial detectors has to be evaluated. Therefore,

$$|\nu_i(r)\rangle = e^{-i\tilde{H}r}|\nu_i^e\rangle \tag{A1}$$

must be integrated (cf. Eq. 5). $|\nu_i^e\rangle$ denotes the initial electron-neutrino state given by Eq. (8). The evolution starts at a point inside the Sun given by r_0 and ϑ_0 (see Fig. 17). The neutrino path has then to be followed through Sun, space and, if necessary, Earth arriving at the detector at the day D under the zenith angle ζ. From the final state $|\nu_i^{\mathrm{f}}\rangle$ the electron-neutrino survival probability $P_{e\to e}(\Delta m^2_{12}/E, \Delta m^2_{13}/E, \sin^2 2\Theta_{12}, \sin^2 2\Theta_{13}, r_0, \vartheta_0, D, \zeta)$ is derived using the relation

$$P_{e\to e} = \left|\langle \nu_i^{\mathrm{f}}|\nu_i^e\rangle\right|^2 . \tag{A2}$$

Since none of the detectors is able to discriminate between ν_μ and ν_τ, the contribution of these neutrino families is simply given by $1 - P_{e\to e}$.

First, the neutrino paths through the Sun are considered. Since N_{e}, and thus also the Hamiltonian $\tilde{\mathcal{H}}$, is a function of r the integration of Eq. (A1) is performed piecewise. For this purpose, the interior of a solar model is subdivided into a grid equally spaced in electron density (about 500 grid points). By approximating the electron density between two neighboring grid point linearly, Eq. (A1) can be solved analytically. Thereby the neutrino state can be followed through the whole solar interior. Furthermore, the accuracy is improved by increasing the grid density near the resonance (Eq. 11).

Most of the neutrinos emerge between $0 < r_0 \lesssim 0.4R_\odot$ and $0 \le \vartheta_0 \le \pi$. If the MSW-resonance lies within this region, it is crucial to carefully calculate the paths for neutrinos with different r_0, as the more centrally produced neutrinos may undergo a MSW-conversion, while the outermost are hardly influenced by the matter. Paths with $\vartheta_0 > \pi/2$ may even twice cross the MSW-resonance region. The contribution of a neutrino emerging at an angle ϑ_0 and radius r_0 to the total flux originating in this shell is given by

$$\Omega(\vartheta_0) = 0.5\sin(2\vartheta_0)\,\mathrm{d}\vartheta_0$$

for $0 \le \vartheta_0 \le \pi/2$. From the symmetry around the plane $\vartheta_0 = \pi/2$ it follows that $\Omega(\vartheta_0) = \Omega(\pi - \vartheta_0)$.

Since all neutrinos cross the shell $0.4R_\odot \lesssim r_0 \le R_\odot$ a set of paths through this area is established (generally

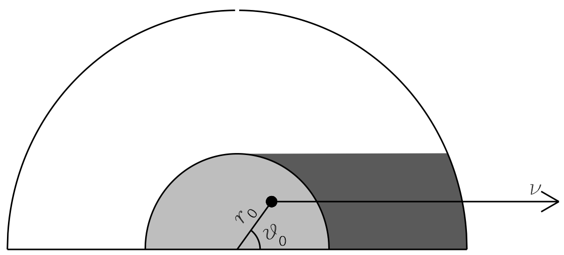

FIG. 17. Illustrating the definition of r_0 and ϑ_0. The light shaded region reflects the region of neutrino production, the dark shaded is covered by about 50 different paths (see text) with direction to the Earth (arrow labeled ν).

about 50 equally spaced in $\sin\vartheta_0$) on which $\exp(-i\tilde{\mathcal{H}}r)$ is calculated numerically by adding up the solutions in each region linearized in N_{e}. Thus, a set of matrices is obtained $\mathcal{S}_\odot(\sin\vartheta_0)$ which describes the evolution from $r \approx 0.4R_\odot$ to the solar surface. By this means the neutrino state $|\nu_i^\odot(r_0,\vartheta_0)\rangle$ is evaluated by first integrating Eq. (A1) until $r \approx 0.4R_\odot$ and then using that matrix $\mathcal{S}_\odot(\sin\vartheta_0)$, which was calculated for a path closest to the actual path of $|\nu_i(r_0,\vartheta_0)\rangle$. It turns out that calculating solely two paths ($\vartheta_0 = 0$ and π) yields mostly already acceptable results. In this case, of course, only one matrix $S_\odot(0)$ is needed.

Now, the state $|\nu_i^\odot(r_0,\vartheta_0)\rangle$ is followed until the surface of the Earth using the equation for the vacuum oscillations (Eq. 6). Since the Earth's orbit is eccentric, different days D during a year are discriminated (about 20 from perihelion to aphelion). In a final step the rotation of the Earth and thus the different paths of a neutrino through the Earth's interior during one day are considered. Here a procedure similar to the shell outside the fusion region of the Sun is applied: A set of about 30 matrices $\mathcal{S}_{♀}(\sin\zeta)$ is calculated integrating $\exp(-i\tilde{\mathcal{H}}r)$ through the Earth.

By applying finally Eq. (A2) the survival probability $P_{\mathrm{e}\to\mathrm{e}}(r_0,\vartheta_0,D,\zeta)$ for a certain set of parameters $\Delta m_{12}^2/E$, $\Delta m_{13}^2/E$, $\sin^2 2\Theta_{12}$, $\sin^2 2\Theta_{13}$ is obtained. This is the basic quantity from which the final event rates are calculated.

Since the experiments provide data binned in certain periods (e.g. day, night, annual seasons or a whole year) resp. in certain ranges of the zenith angle, $P_{e\to e}(r_0,\vartheta_0,D,h)$ first has to be integrated using the zenith-angle weights $W_\lambda(\zeta,D)$ (see e.g. [13]) for each period D at the detector latitude λ.

After that, $P_\lambda^k(r_0,\vartheta_0)$ is folded with the radial distribution $\Phi_{\mathrm{r}}(r_0)$ of the neutrino sources inside the Sun and the angle weights Ω discriminating the different neutrino types (pp, ^{7}Be, ^{8}B etc., denoted by the superscript f). The event rates in the detectors are obtained by finally folding P_λ^f with the energy spectrum of each neutrino type Φ_{E}^f and the detector response function $\Xi_i(E)$, and summing up the contribution of all neutrino types. This yields

$$N_i = \sum_f \int P_\lambda^f \, \Xi_i(E')\, \Phi_{\mathrm{E}}^f(E')\, \mathrm{d}E', \qquad \text{(A3)}$$

where i is either Ga or Cl. The detector response function for the Homestake detector can be found e.g. in [56] and for the Ga-detectors in [57].

In Super-Kamiokande, Borexino and SNO the energy spectrum of the recoil-electron (resp. recoil-deuterium) spectrum can be measured at least within certain energy bins. Furthermore, SNO is able to discriminate CC- and NC-events, while Super-Kamiokande and Borexino measure the total number of events arisen by any neutrino flavour. According to [49] the response function for these type of experiments with the recoil-electron energy between T_0 and T_1 is given by

$$\Xi_\Upsilon(E,T_0,T_1) = \int_{T_0}^{T_1} \mathrm{d}T \int \mathrm{d}T' R(T,T') \frac{\mathrm{d}\sigma_\Upsilon(E,T')}{\mathrm{d}T'}, \qquad \text{(A4)}$$

where with

$$R(T,T') = \frac{1}{\sqrt{2\pi}\Delta_{\mathrm{T}'}} \exp\left(-\frac{(T'-T+\delta)^2}{2\Delta_{\mathrm{T}'}^2}\right)$$

the energy resolution of the detector is included. Therein δ accounts for a possible uncertainty in the absolute energy calibration and Δ_{T} is the energy resolution width following the photon statistics which yields

$$\Delta_{\mathrm{T}} = \Delta_{10}\sqrt{\frac{T}{10\,\mathrm{MeV}}}$$

with Δ_{10} being the energy resolution at 10 MeV. The parameters Δ_{10} and δ for Super-Kamiokande, SNO and Borexino are summarized in Table V.

TABLE V. Energy resolution parameters used in the present work. The values for Super-Kamiokande and SNO are taken from [49]. For Borexino Δ_1 the energy resolution width at 1 MeV provided by L. Oberauer (private communication) is quoted.

	Super-K	SNO	Borexino
Δ_{10}	1.6 MeV	1.1 MeV	47 keV
δ	10 keV	100 keV	—

The cross sections $\frac{\mathrm{d}\sigma_\Upsilon(E,T)}{\mathrm{d}T}$ for Super-Kamiokande and Borexino were calculated following the description in [58]. Υ denotes either ν_e and ν_μ (or equivalent ν_τ) for the interaction of these neutrino flavours with Super-Kamiokande and Borexino or CC resp. NC for the reaction type in the SNO detector. With $\Xi_\Upsilon(E,T_0,T_1)$ given by Eq. (A4) the event rates in Borexino resp. Super-Kamiokande are obtained from

$$N_i^k(T_0,T_1) = \sum_f \int \Big[(1-P_\lambda^{k,f})\, \Xi_{\nu_\mu}(E',T_0,T_1) + P_\lambda^{k,f}\, \Xi_{\nu_e}(E',T_0,T_1)\Big]\, \Phi_{\mathrm{E}}^{\mathrm{f}}(E')\, \mathrm{d}E', \qquad \text{(A5)}$$

while the number of CC- and NC-events in SNO is defined analogous to the Gallium and Chlorine detector (Eq. A3). With the threshold energy being greater than 5 MeV only the sum over ^{8}B- and hep-neutrinos has to be performed in Super-Kamiokande and SNO.

[1] R. Davis Jr., D. S. Harmer, and K. C. Hoffman, Phys. Rev. Lett. **20**, 1205 (1968).
[2] W. A. Dziembowski, P. R. Goode, A. A. Pamyatnykh, and R. Sienkiewicz, Astrophys. J. **445**, 509 (1994); S. Basu *et al.*, *ibid.* **460**, 1064 (1996); H. M. Antia, Astron. Astrophys. **307**, 609 (1996); S. Basu, M. H. Pinsonneault, and J. N. Bahcall, Astrophys. J. **529**, 1084 (2000).
[3] H. Schlattl, A. Weiss, and H.-G. Ludwig, Astron. Astrophys. **322**, 646 (1997).
[4] J. N. Bahcall, S. Basu, and M. H. Pinsonneault, Phys. Lett. B **433**, 1 (1998).
[5] M. Gabriel, Astron. Astrophys. **309**, 939 (1996); O. Richard, S. Vauclair, C. Charbonnel, and W. A. Dziembowski, *ibid.* **312**, 1000 (1996).
[6] P. Anselmann *et al.* (the GALLEX collaboration), Phys. Lett. B **285**, 376 (1992); the GALLEX-collaboration measured solar neutrinos from May 1991 to January 1998 interrupted by some maintenance work and calibration experiments. In July 1998 the facilities were taken over by the newly formed GNO-group (Gallium Neutrino Observatory). After an extension of the Gallium-target to 60 t and further technical improvements the detector has been taking data again since the spring of 1999.
[7] J. N. Abdurashitov *et al.* (the SAGE collaboration), Phys. Lett. B **328**, 234 (1994).
[8] N. Hata and P. Langacker, Phys. Rev. D **52**, 420 (1995).
[9] H. Schlattl, Ph.D. thesis, Technical University Munich, 1999.
[10] B. Pontecorvo, Zh. Eksp. Teor. Fiz. **53**, 1717 (1967) [Sov. Phys. JETP **26**, 984 (1968)].
[11] S. P. Mikheyev and A. Yu. Smirnov, Yad. Fiz. **42**, 1441 (1985) [Sov. Jour. Nucl. Phys. **42**, 913 (1985)]; L. Wolfenstein, Phys. Rev. D **17**, 2369 (1978).
[12] N. Hata and P. Langacker, Phys. Rev. D **56**, 6107 (1997); H. Schlattl, A. Bonanno, and L. Paternò, *ibid.* **60**, 113002 (1999); J. N. Bahcall, P. I. Krastev, and A. Yu. Smirnov, Phys. Lett. B **477**, 401 (2000).
[13] J. N. Bahcall and P. I. Krastev, Phys. Rev. C **56**, 2839 (1997).
[14] Y. Fukuda *et al.* (the Super-Kamiokande collaboration), Phys. Rev. Lett. **82**, 2430 (1999).
[15] Y. Fukuda *et al.* (the Super-Kamiokande collaboration), Phys. Rev. Lett. **82**, 1810 (1999).
[16] J. N. Bahcall, P. I. Krastev, and A. Yu. Smirnov, Phys. Rev. D **58**, 096016 (1998).
[17] R. Schiavilla, R. B. Wiringa, V. R. Pandharipande, and J. Carlson, Phys. Rev. C **45**, 2628 (1992).
[18] J. N. Bahcall, P. I. Krastev, and A. Yu. Smirnov, Phys. Rev. D **60**, 093001 (1999).
[19] G. L. Fogli, E. Lisi, and D. Montanino, Phys. Rev. D **54**, 2048 (1996).
[20] G. L. Fogli, E. Lisi, D. Montanino, and A. Palazzo, hep-ph/9912231 (1999); T. Teshima, T. Sakai, and O. Inagaki, Int. J. Mod. Phys. A **14**, 1953 (1999); J. S. Kim and C. W. Kim, hep-ph/9909428 (1999).
[21] G. G. Raffelt, *Stars as Laboratories for Fundamental Physics* (University of Chicago Press, Chicago, 1996).
[22] S. T. Petcov, Phys. Lett. B **214**, 259 (1988).
[23] V. Barger, K. Whisnant, S. Pakvasa, and R. J. N. Philips, Phys. Rev. D **22**, 2718 (1980).
[24] T. Ohlsson and H. Snellman, J. Math. Phys. (to be published).
[25] J. Lundell and H. Snellman, Phys. Lett. B **470**, 163 (1999).
[26] A. Friedland, hep-ph/0002063 (2000).
[27] A. de Gouvêa, A. Friedland, and H. Murayama, hep-ph/0002064 (2000).
[28] C. Caso *et al.* (Particle Data Group), Eur. Phys. J. C **3**, 1 (1998).
[29] M. C. Gonzalez-Garcia and C. Peña-Garay, hep-ph/0002186 (2000).
[30] J. Bouchez *et al.*, Z. Phys. C **32**, 499 (1986); S. P. Mikheyev and A. Yu. Smirnov, in *Proceedings of the 7th Moriond Workshop on New and Exotic Phenomena*, edited by O. Fackler and T. T. Vân (Frontières, Paris, 1987), p. 405; M. Spiro and D. Vignaud, Phys. Lett. B **242**, 279 (1990).
[31] T. K. Kuo and J. Pantaleone, Phys. Rev. Lett. **57**, 1805 (1986).
[32] H. Schlattl and A. Weiss, Astron. Astrophys. **347**, 272 (1999).
[33] F. J. Rogers, F. J. Swenson, and C. A. Iglesias, Astrophys. J. **456**, 902 (1996).
[34] C. A. Iglesias and F. J. Rogers, Astrophys. J. **464**, 943 (1996).
[35] E. G. Adelberger *et al.*, Rev. Mod. Phys. **70**, 1265 (1998).
[36] A. A. Thoul, J. N. Bahcall, and A. Loeb, Astrophys. J. **421**, 828 (1994).
[37] B. Freytag, H.-G. Ludwig, and M. Steffen, Astron. Astrophys. **313**, 497 (1996).
[38] M. Canuto and I. Mazzitelli, Astrophys. J. **370**, 295 (1991); **389**, 724 (1992).
[39] W. Hampel *et al.* (the GALLEX collaboration), Phys. Lett. B **447**, 127 (1999); J. N. Abdurashitov *et al.* (the SAGE collaboration), Phys. Rev. C **60**, 055801 (1999).
[40] B. T. Cleveland *et al.*, Astrophys. J. **496**, 505 (1998).
[41] M. Nakahata, talk given at Trento'99 Workshop on "Nuclear Reactions in Stars and in the Laboratory" (unpublished).
[42] S. Basu, Mon. Not. R. Astron. Soc. **298**, 719 (1998).
[43] J. Christensen-Dalsgaard *et al.*, Science **272**, 1286 (1996).
[44] S. Degl'Innocenti, S. Dziembowski, W. A. Fiorentini, and B. Ricci, Astropart. Phys. **7**, 77 (1997).
[45] A. M. Dziemonski and D. L. Anderson, Phys. Earth Planet. Interior **25**, 207 (1981).
[46] V. Berezinsky, G. Fiorentini, and M. Lissia, INFNCA-TH9815, hep-ph/9811352.
[47] Q. Y. Liu and S. T. Petcov, Phys. Rev. D **56**, 7392 (1997).
[48] A. de Gouvêa, A. Friedland, and H. Murayama, Phys. Rev. D **60**, 093011 (1999).
[49] J. N. Bahcall, P. I. Krastev, and E. Lisi, Phys. Rev. C **55**, 494 (1997).
[50] J. N. Bahcall, P. I. Krastev, and A. Yu. Smirnov, hep-ph/0002293 (2000).
[51] Y. Fukuda *et al.* (the Super-Kamiokande Collaboration), Phys. Rev. Lett. **82**, 2644 (1999).

[52] T. Sakai and T. Teshima, hep-ph/9901219 (1999).
[53] C. Athanassopoulos *et al.* (the LSND Collaboration), Phys. Rev. C **58**, 2489 (1998).
[54] K. Eitel, in *Lake Louise Winter Institute 1999* (Lake Louise, 1999), for the KARMEN Collaboration.
[55] J. W. F. Valle, in *Corfu Summer Institute on Elementary Particle Physics, Kerkyra, Greece, 6-20 Sep 1998*, edited by I. Antioniadis, G. Koutsoumbas, N. Tracas, and G. Zoupanos (JHEP, 1998).
[56] J. N. Bahcall *et al.*, Phys. Rev. C **54**, 411 (1996).
[57] J. N. Bahcall, Phys. Rev. C **56**, 3391 (1997).
[58] J. N. Bahcall, M. Kamionkowski, and A. Sirlin, Phys. Rev. D **51**, 6146 (1995).